Comparative Brain-Wide Mapping of Isoflurane and Ketamine-Activated Nuclei and Functional Networks

Keywords: c-Fos; Isoflurane; Ketamine; Functional network.

Abstract

Ketamine (KET) and isoflurane (ISO) are two widely used general anesthetics, yet their distinct and shared neurophysiological mechanisms remain elusive. In this study, we conducted a comparative analysis of KET and ISO effects on c-Fos expression across the brain, utilizing principal component analysis (PCA) and c-Fos-based functional network analysis to evaluate the responses of individual brain regions to each anesthetic. Our findings demonstrate that KET significantly activates cortical and subcortical arousal-promoting nuclei, with the somatosensory cortex (SS) serving as a hub node, corroborating the top-down general anesthesia theory for dissociative anesthesia. In contrast, ISO activates the nuclei in the hypothalamus and brainstem, with the locus coeruleus (LC) as a hub node, implying a bottom-up mechanism for anesthetic-induced unconsciousness. Notably, the coactivation of sleep-wakefulness regulation, analgesia-related, neuroendocrine-related nuclei (e.g., prelimbic area (PL) and infralimbic areas (ILA), and the anterior paraventricular nucleus (aPVT), Edinger-Westphal nucleus (EW), locus coeruleus (LC), parabrachial nucleus (PB), solitary tract nucleus (NTS)) by both anesthetics underscores shared features such as unconsciousness, analgesia, and autonomic regulation, irrespective of their specific molecular targets. In conclusion, our results emphasize the distinct actions of KET and ISO while also uncovering the commonly activated brain regions, thus contributing to the advancement of our understanding of the mechanisms underlying general anesthesia.

Introduction

Despite considerable investigation into the molecular targets, neural circuits, and functional connectivity associated with various anesthetics, our comprehension of their effects on overall brain activity continues to be limited and incomplete [1]. At the molecular level, ketamine (KET) and isoflurane (ISO) interact with N-methyl-D-aspartate (NMDA) and gamma-aminobutyric acid type A (GABAa) receptors, respectively, modulating neuronal excitability and ultimately leading to a loss of consciousness [2]. In systems neuroscience,

the neural mechanisms of anesthetic induced unconsciousness involve both top-down and bottom-up processes [3, 4]. As evidenced by in vivo electrophysiology or functional magnetic resonance imaging (fMRI) studies, the top-down paradigm illustrates that anesthetics induce unconsciousness by disrupting corticocortical and corticothalamic circuits responsible for neural information integration, while peripheral sensory information can still be conveyed to the primary sensory cortex [5, 6]. The bottom-up approach, exemplified by ISO, involves the activation of sleep-promoting nuclei like ventral lateral preoptic nucleus (VLPO) and inhibition of arousal centers in the brainstem and diencephalon, supporting the shared circuits of sleep and anesthesia [7, 8]. However, the limited spatial resolution of fMRI studies and the inability of EEG to capture specific brainstem nuclei hinder the acquisition of comprehensive whole-brain information. Although a substantial body of knowledge has been amassed, our understanding of the reciprocal responses among different brain regions during general anesthesia remains relatively sparse and fragmented. To bridge these gaps, further investigation using advanced techniques that can capture the whole-brain dynamics is needed to elucidate the complex interactions and shared mechanisms between various anesthetics.

Neuronal extracellular stimulation typically results in the elevation of adenosine 3',5'-cyclic monophosphate (cAMP) levels and calcium influx, ultimately leading to the upregulation of immediate early genes (IEGs) such as c-fos [9, 10]. The translation product of c-fos, c-Fos protein, offers single-cell spatial resolution and has been utilized as a biomarker to identify anesthetic-activated brain regions [11]. Previous investigations of c-Fos expression throughout the brain demonstrated that GABAergic agents inhibited cortical activity while concurrently activating subcortical brain regions, including the VLPO, median preoptic nucleus (MnPO), lateral septal nucleus (LS), Edinger-Westphal nucleus (EW), and locus coeruleus (LC) [12-15]. In contrast, KET was shown to provoke wake-like c-Fos expression and intense augmentation of c-Fos expression in various brain regions at clinical dosages (75-100 mg/kg) [13]. It is important to note that these experiments administered KET at lights-on and GABAa receptor agonists at lights-off, potentially introducing circadian influences for direct comparison of ISO and

KET. Moreover, it has been revealed that state of general anesthesia is not determined by activity in individual brain areas, but emerges as a global change within the brain. This change involves the activation of lateral habenular nucleus (LHb), VLPO, supraoptic nucleus (SON), and central amygdaloid nucleus (CeA), which are essential for anesthetics induced sedation, unconsciousness, or analgesia [7, 16-18]. However, brain-wide mapping and comparison of distinct anesthetic (KET and ISO) activated nuclei at a cellular level have not been fully elucidated.

In this study, we examined the distribution of nuclei activated by ISO and KET in 987 brain regions using immunochemical labeling and a customized MATLAB software package, which facilitated signal detection and registration to the Allen Mouse Brain Atlas reference [19]. We compared whole-brain c-Fos expression induced by KET and ISO through principal component analysis (PCA) and calculated inter-regional correlations by determining the covariance across subjects for each brain region pair. We then extracted significantly positively correlated brain regions to construct functional networks and performed graph theory-based network analyses to identify hub nodes. Our results uncovered distinct yet overlapping whole-brain activation patterns for KET and ISO.

Results

A comparison of the activation patterns of c-Fos in 53 brain areas in response to ISO and KET

To examine the pattern of c-Fos expression throughout the brain, 1.5% ISO was continuously ventilated, or 100 mg/kg KET was administered 90 minutes before harvesting (Figure 1A). Concurrently, to quantitatively assess brain states across the four groups, we utilized electroencephalography (EEG) and electromyography (EMG) recordings (Figure 1—figure supplement 1). The depth of anesthesia was evaluated based on the power ratio of the EEG within the delta (0.5–4 Hz) and theta (6–10 Hz) frequency bands, combined with the changes in the EMG [20]. Our findings showed that ISO and KET notably elevated EEG power ratio while reducing EMG power, suggesting both drugs induced a loss of consciousness. The raw images of brain slices were aligned to the Allen Mouse Brain Atlas (Figure 1B). Based on the standard mouse atlas available at http://atlas.brain-map.org/, the mouse brain

was segmented into nine hierarchical levels, totaling 987 regions. The primary level consists of grey matter, the secondary of the cerebrum, brainstem, and cerebellum, and the tertiary includes regions like the cerebral cortex and cerebellar nuclei, among others. Some regions extend to the 8th and 9th levels. Our initial statistical comparison was conducted on the fifth level, which is composed of 53 subregions, as detailed in Supplementary Table 1 (Figure 1B) [21]. To differentiate c-Fos expression patterns across groups, we calculated the c-Fos density for each brain region, divided it by the overall brain c-Fos density, and then applied a logarithmic transformation. The transformed values were used for principal component analysis (PCA) (Figure 2A). The KET and ISO groups were distinctly delineated by the top two principal components. Notably, the KET-induced c-Fos expression manifested a positive association with principal component 1 (PC1), clustering around +2.5, which represented 30.72% of the total variance. In contrast, it exhibited a negative correlation with principal component 2 (PC2), clustering near -2.0, which contributed to 25.89% of the variance. On the other hand, ISO displayed a positive correlation with PC2, clustering at approximately +2.5, while its association with PC1 was neutral, near 0. Figure 2B illustrates the component coefficients of PC1 and PC2 for each brain region. Dots represent the top 25% of brain regions based on the absolute values of their component coefficients, signifying the most influential regions. KET, predominantly positively correlated with PC1, is associated with the activation of cortical regions (as evidenced by positive PC1 coefficients in MOB, AON, MO, ACA, and ORB) and the inhibition of subcortical areas (indicated by negative coefficients). On the other hand, ISO, with its notable association with PC2, showed top 25% positive coefficients in PALc, LSX of CNU, cortical ILA, and hypothalamic PVZ, while its negative coefficients were found primarily in cortical regions. These observations underscore that KET and ISO exhibit distinct patterns of brain region activation. KET displays cortical activation and subcortical inhibition, whereas ISO shows a contrasting preference, activating the cerebral nucleus (CNU) and the hypothalamus while inhibiting cortical areas. To reduce inter-individual variability, we normalized c-Fos$^+$ cell counts in each brain area by dividing them by the total c-Fos$^+$ cells in the entire brain (Figure 2C), Subsequently, we directly compared the differences between ISO

and KET with their respective control groups. In line with PCA results**,** KET significantly activated the isocortex (16.55 ± 2.31 vs. 40.13 ± 1.97, $P < 0.001$) and reduced the proportion of c-Fos$^+$ cells in the hypothalamus (14.88 ± 2.18 vs. 4.03 ± 0.57, $P = 0.001$) and midbrain (21.87 ± 2.74 vs. 6.48 ± 1.06, $P = 0.005$) compared to the saline group. In contrast, the proportion of c-Fos$^+$ cells induced by ISO were mainly observed in the striatum and hypothalamus compared to the home cage group, specifically in the periventricular zone (PVZ) (2.330 ± 0.759 vs. 6.63 ± 0.84, $P = 0.015$) and lateral zone (LZ) (2.82 ± 0.3 vs. 5.59 ± 0.75, $P = 0.002$) of the hypothalamus, as well as STRv (0.59 ± 0.10 vs. 2.77 ± 0.40, $P < 0.002$) and LSX (1.93 ± 0.59 vs. 5.11 ± 0.41, $P = 0.004$) of the striatum (Figure 2C and Table 1). **In** summary, our findings reveal that KET predominantly affects cortical regions, whereas isoflurane mainly targets subcortical areas, specifically the striatum, and hypothalamus. These results demonstrate distinct patterns of brain region activation for each anesthetic agent.

Similarities and differences in ISO and KET activated c-Fos brain areas.

To elucidate the c-Fos expression patterns induced by ISO and KET more clearly, we refined our focus from the initial 53 brain regions to a more granular examination of subregions, culminating in a comprehensive assessment of 201 distinct areas. We conducted a PCA on the logarithmic ratio of c-Fos density across these regions to discern variance among the groups (Figure 3). The KET group predominantly clustered around +7 on PC1 and approximately 0 on PC2, whereas the ISO group clustered around +4 on PC2 and -3 on PC1. KET displayed a strong positive correlation with PC1, accounting for 28.97% of the variance. In contrast, ISO negatively correlated with PC1 and positively with PC2, which accounted for 15.54% of the variance (Figure 3A). These findings underscore the distinct features between the ISO and KET groups, with the top two principal components effectively separating them. Further analysis of PC coefficients in each brain region showed (Figure 3B) that KET, positively associated with PC1, mainly activates the cerebral cortex (CTX) areas including the visceral area (VISC), claustrum (CLA), dorsal peduncular area (DP), orbital area (ORB), and temporal association areas (TEA), while inhibiting the hypothalamus, midbrain, and hindbrain. In

contrast, ISO is negatively correlated with PC1, suggesting that the cortical areas activated by KET are inhibited by ISO. Additionally, ISO has a positive association with PC2 and is predominantly related to the activation of hypothalamic regions, such as the ventrolateral preoptic nucleus (VLPO), suprachiasmatic nucleus (SCH), tuberal nucleus (TU), medial preoptic area (MPO), and supraoptic nucleus (SON), as well as certain nuclei in the central nucleus (CNU). KET primarily activates regions within the cerebral cortex (CTX) and inhibits areas within the hypothalamus, midbrain, and hindbrain, aligning with the top-down mechanism suggesting anesthetic agents influence cortical and thalamocortical circuits [4]. Conversely, ISO activates hypothalamic areas while suppressing the cortex, midbrain, and hindbrain, consistent with the bottom-up mechanism. Figure 3C summarizes these distinctive responses, implying that anesthetic agents like KET and ISO modulate consciousness by targeting particular brain regions and neural circuits.

Identification of brain regions activated by KET

We further employed quantitative methods to identify the brain regions activated by KET across the entire brain. Our findings concur with previous studies: numerous cortical regions associated with somatosensory, auditory, visual, and movement were activated (Figure 4A and C, Supplementary Figure 1, Supplementary Table 2). Additionally, we identified several innovative observations that enrich the current understanding in this field. To provide a clearer overview of our findings, we categorized the activated brain areas into different functional groups: (1) Arousal and REM sleep regulation: Several nuclei associated with arousal were activated, including the prelimbic area (PL), infralimbic cortex (ILA), paraventricular nucleus of the thalamus (PVT), dorsal raphe (DR), and sublaterodorsal nucleus (SLD). Prior evidence indicates that the PL/ILA and PVT regions play a role in regulating arousal in both cortical and subcortical areas[22, 23]. Additionally, dopaminergic neurons within the DR have been identified as vital components of wake-promoting pathways [24]. In the context of REM sleep, the sublaterodorsal nucleus (SLD) stands out for its role in stabilization[25]. (2) Pain modulation, KET significantly activated pain-related areas such as the anterior cingulate cortex (ACA) in the cortex [26], the anterior pretectal nucleus (APN) in the

thalamus, which is known to be involved in managing chronic pain [27], and the anterior periaqueductal gray (PAG) region and medial prefrontal cortex (mPFC), both part of the endogenous pain inhibitory pathway [28, 29]. Additionally, the activation of the locus coeruleus (LC) in the midbrain may contribute to KET's analgesic effects [30]. (3) Neuroendocrine regulation: The paraventricular hypothalamic nucleus (PVH) and supraoptic nucleus (SON), which are neuroendocrine-related regions, were also activated [18, 31]. (4) Movement: Subcortical nuclei associated with movement, such as the subthalamic nucleus (STN) and nucleus incertus (NI), were prominently activated by KET administration [32, 33]. (5) Connectivity: We observed significant activation of the nucleus reuniens (Re) located in the thalamus, which receives substantial afferent input from limbic structures and serves as a connector linking the hippocampus to the medial prefrontal cortex [34]. While our functional categorization offers a simplified overview, it's worth noting that each activated brain region may have multifaceted roles beyond this classification. In summary, our study identified extensive activation of cortical and subcortical nuclei during KET anesthesia, encompassing regions related to arousal, pain modulation, neuroendocrine regulation, movement, and connectivity.

Identification of brain regions activated by ISO

In our study, we aimed to identify brain regions activated by ISO and compare these with those activated by KET. We began by summarizing previously reported ISO activated nuclei, including PIR, LSd/LSv, CeA in the cortex and striatum, and VLPO, MnPO, EW, NTS, LC, ventral group of the dorsal thalamus (VeN), and area postrema (AP) in the hypothalamus and midbrain (Supplementary Table 3). We subsequently conducted a comprehensive MATLAB-based analysis of c-Fos expression throughout the entire brain, uncovering previously undetected activated nuclei (Figure 5A, Supplementary Figure 2). Newly identified activated nuclei in the CTX and the CNU included PL/ILA and ENT, aPVT in the thalamus, TU, ARH, PVi, and PVH in the hypothalamus, and PB in the hindbrain. All nuclei activated by ISO in this study were functionally classified and depicted in Figure 5C. Our results confirmed the activation of several brain regions involved in arousal-related nuclei, such as the prelimbic area (PL) and infralimbic areas (ILA), and the

paraventricular nucleus (PVT) [22, 23]. Additionally, we observed activation in previously reported analgesia-related nuclei, including CeA and LC, as well as the parabrachial nucleus (PB) [18, 30, 35]. We also found activation in neuroendocrine function-related nuclei of the hypothalamus, such as TU, PVi, ARH, PVH, and SON. Moreover, we identified activations related to ISO induced side effects, such as in the piriform cortex (PIR) [36] and ENT [37], which may be stimulated by ISO odor, and the solitary tract nucleus (NTS), potentially responsible for ISO induced vomiting [38]. The only activated nucleus in the midbrain was the Edinger-Westphal nucleus (EW). Recent research has found that sevoflurane activates EW and is involved in sleep induction and maintenance of anesthesia, suggesting its crucial role in general anesthesia [39]. By comparing the ISO and KET induced c-Fos expression, we summarized the brain regions activated by both anesthetics in Figure 5D. Despite variations in molecular targets, the coactivation of regions such as PL/ILA, aPVT, CeA, PVH, SON, EW, PB, LC, and NTS by both ISO and KET suggests an overlapping neuronal circuitry that influences sleep-wake regulation, analgesia, and neuroendocrine functions. This shared neural circuitry may potentially offer a common mechanism across the two anesthetics for the maintenance of general anesthesia.

Network generation and Hub identification

Previous research has established that general anesthesia is mediated by various brain regions [7, 16-18]. c-Fos expression serves as an indicator of neuronal activity, providing a single index of activation per region per animal. By examining the covariance of c-Fos expression across animals within each group, we can infer interactions between brain regions and identify functional networks engaged during general anesthesia [40]. Consequently, we initially incorporated a total of 63 brain regions, including nuclei that were significantly activated by ISO and KET (as indicated by positive findings in Figures 4 and 5) and those previously reported to be associated with the mechanisms of general anesthesia and sleep-wakefulness [41]. Highly correlated activities across different brain regions are presumed to constitute components of a functional network, reflecting the complex interplay of brain areas during general anesthesia. Using c-Fos expression as a marker for neuronal activity and calculated a comprehensive set of interregional correlations for four

groups. The matrices exhibited interregional correlations for the number of c-Fos-positive cells in each condition (Figure 6A). Network graphs were generated by extracting Pearson's coefficients > 0.82, as well as significant positive correlations ($P < 0.05$), from these matrices to construct functional brain networks (Figure 6B). Compared to the control group, isoflurane (ISO) slightly decreased interconnections between regions (network density: 0.13 vs. 0.10; edges: 267 vs. 198), with no significant difference in mean interregional correlation coefficients between the ISO group and the home cage group (Fisher $Z = -0.018$, $P = 0.98$). Conversely, ketamine (KET) significantly increased the network's connectivity density (network density: 0.13 vs. 0.47; edges: 265 vs. 1008) and showed a significant increase in mean interregional correlation coefficients compared to the saline group (Fisher $Z = 3.54$, $P < 0.001$) (Figure 6C). These findings suggest that ISO may exert a mild inhibitory effect on functional network connectivity, whereas KET appears to enhance interregional correlation following administration (Figure 6D).

Hubs are nodes that occupy critical central positions within the network, enabling the network to function properly. To determine the brain regions that serve as the hubs for ISO and KET induced functional networks, we calculated each node's degree (the number of links that connect it) and betweenness centrality (the fraction of all shortest paths in the network that contain a given node). Nodes with high degree and betweenness centrality values typically exhibit many connections. We ranked each node according to its degree and betweenness centrality and extracted nodes with a rank greater than the 80th percentile in its network (Figure 7). Additionally, we segmented the functional network into non-overlapping modules using a spectral community detection algorithm and calculated the within-modal degree Z-score (the degree of nodes within a module, which indicates within-module connectivity) as well as participation coefficients (the distribution of the edges of a node between other modules, which indicates within-module connectivity) [42]. Nodes with relatively high values for both parameters were considered relatively significant within and outside the network module. We classified nodes with participation coefficients > 0.4 and Z scores > 1 as connector hubs [43]. The LC, exhibiting elevated degree and betweenness centrality as well as relatively higher Z-scores and participation coefficients,

may play a pivotal role in mediating isoflurane-induced general anesthesia, given its known involvement in arousal, attention, and analgesia. In contrast, the somatosensory cortex (SS) functions as a connector hub in the KET group, indicating its integrative and coordinating role in ketamine-induced dissociative anesthesia (Figure 7D). The LSc served as the central hub in the saline group (Figure 7C). No significant findings were observed in the within-modal degree Z-score and participation coefficient analyses for the home cage group. However, the analysis did reveal a relatively high degree and betweenness centrality of APNs (Figure 7A), suggesting that the within-module connections are relatively independent, or that the pathways of inter-module information transmission do not depend on specific connector nodes.

Discussion

In this study, we conducted a comparative analysis of the effects of two general anesthetics, isoflurane (ISO) and ketamine (KET), on c-Fos expression throughout the brain. By employing principal component analysis (PCA), we were able to thoroughly examine the responses of individual brain regions to each anesthetic agent. Our findings reveal that KET dominantly activates the cerebral cortex yet suppresses subcortical regions, reflecting a top down mechanism of action, while ISO predominantly stimulates subcortical brain regions with relative cortical inhibition, substantiating its bottom up mechanism of action [3, 4]. Further functional analysis of brain networks, based on c-Fos expression, identified the somatosensory cortex (SS) and the locus coeruleus (LC) as central nodes for KET and ISO, respectively, highlighting the crucial roles of LC and SS under ISO and KET induced unconsciousness.

Our results demonstrate that ISO activates the sleep-promoting VLPO nucleus, the aPVT-infralimbic loop [23], and broadly inhibits the cortex, supporting a bottom-up mechanism of ISO induced unconsciousness. Nonetheless, our findings also reveal the activation of arousal related nuclei, such as PB and LC, which implies that the influence of isoflurane on consciousness may not solely rely on suppressing arousal centers, but rather through a more intricate relationship than formerly recognized. Identifying cell types and their dynamic changes during anesthesia will be crucial for clarifying their role in ISO induced unconsciousness.

While c-Fos-based functional network analysis offers lower temporal resolution, its single-cell resolution across the entire brain allows for the inclusion of midbrain and hindbrain regions, supplementing previous fMRI analyses. Our observations reveal that ISO mildly inhibits network density, and through graph theoretical analysis, we identify the LC as a highly connected hub, highlighting the critical role of the brainstem in ISO induced general anesthesia. The LC performs a wide range of functions in mice, including arousal, pain modulation, attention, stress response, and neuroprotection. Studies have shown that chemical activation of the LC increases whole-brain functional connectivity, attributed to its role as the primary source of norepinephrine (NE) and its extensive influence on nearly the entire brain [44]. The significant LC activation and its central position within the functional network underlying ISO induced unconsciousness suggest that the LC plays a crucial part in maintaining and integrating the entire unconsciousness functional network, emphasizing the involvement of LC in the bottom-up paradigm of ISO induced unconsciousness.

Mashour et al. proposed that anesthesia-induced unconsciousness encompasses not only the modulation of lower-level brain activity but also top down neural processing [3, 4]. Within this top down framework, anesthetics diminish consciousness by interfering with cortical and thalamocortical circuits responsible for neural information integration. Our study discovered that KET administration substantially activated cortical and subcortical arousal-promoting nuclei while concurrently causing relative thalamic suppression, with only the RE and TRS exhibiting activation. This suggests that thalamic inhibition may lead to a reduction in thalamocortical communication, which is characterized by the inability to perceive the external environment and results in disconnection from reality. Graph theoretical analysis also identified the somatosensory cortex (SS) as the hub node of the KET induced functional network. As a critical cortical area, SS is responsible for sensory processing, motor control, and cognitive functions [45]. Previous studies have demonstrated that local KET administration to SS recapitulates the effects of systemic KET on both the switch in pyramidal cell activity and dissociative-like behavior, implying that SS may serve as a key target for KET induced dissociation [46]. Our findings that SS acts as a hub node suggest that KET

may modulate brain network function by influencing connectivity between SS and other brain regions, thereby affecting the behavior and cognitive states of mice. This further supports the significance of cortical areas during KET anesthesia.

Identifying shared neural features between KET and ISO is essential for understanding anesthetic-induced unconsciousness. The coactivation of sleep-wake regulation-related regions, such as PL/ILA and aPVT, along with analgesia-related nuclei like CeA, PB, and LC, suggests a shared mechanism for sleep-wake regulation and the common pathways for pain relief. This observation provides valuable insights into the fundamental mechanisms of anesthesia-induced hypnosis and analgesia. Additionally, the coactivation of neuroendocrine-related nuclei, including PVH and SO in the hypothalamus, raises questions about the potential influence of anesthetics on hormonal release and homeostatic regulation. Other coactivated nuclei, such as EW and NTS, warrant further investigation of their roles in anesthesia. In summary, the coactivated nuclei imply a potential shared neuronal circuitry for general anesthesia, encompassing common features like unconsciousness, analgesia, and autonomic regulation, regardless of the specific molecular targets of each drug. Future research could examine coactivated brain regions by the two anesthetics or manipulate identified hub nodes to further understand the mechanisms of general anesthesia. In summary, our study reveals distinct and shared neural mechanisms underlying isoflurane and ketamine anesthesia using c-Fos staining and network analysis. Our findings support "top-down" and "bottom-up" paradigms, and the identification of hub nodes and coactivated brain regions suggests shared neurocircuitry for general anesthesia, providing insights into the mechanisms underlying anesthetic-induced unconsciousness and analgesia.

Methods

Animals

All animal experiments were conducted in accordance with the National Institutes of Health guidelines and were approved by the Chinese Academy of Sciences' Institute of Neuroscience. Adult male wild-type (WT) mice (C57BL/6J) (8-10 weeks old, weight from 22 to 26 g) were purchased from institute-approved vendors (LingChang Experiment Animal Co., China). Mice

were individually housed and maintained on a 12 h:12 h light/dark cycle (lights on at 07:00 a.m. and off at 07:00 p.m.) with food and water available ad libitum.

Drug administration

All experiments occurred between 13:00-14:30 (ZT6–ZT7.5). We adapted mice to handling and the anesthesia chamber (10×15×15 cm) for several days to minimize experimental confound-induced c-Fos induction. Adult male mice were handled for the KET group for 10 min per day with normal saline (NS) injected intraperitoneally (i.p.) for three consecutive days at 13:00. On day five, a randomly chosen mouse received an injection of Ketamine (Gutian Medicine, H35020148), and the control groups (n=8) received the same volume of saline. ISO group (n=6) mice were handled and inhaled 1.5% isoflurane (RWD Life Science, 1903715) at 13:00 on day four in the chamber. Meanwhile, the control groups (n=6) were left undisturbed in their home cages prior to sampling. We confirmed the loss of righting reflex at 5 min after anesthetics exposure. For 90 min after KET injection or ISO inhalation, mice were deeply anesthetized with 5% ISO and transcardially perfused with 35 ml 0.1 M phosphate-buffered saline (PBS) followed by 35 ml 4% paraformaldehyde (PFA). The brains were then removed and postfixed overnight with 4% PFA. Following fixation, the brains were dehydrated for 48 hours with 30% sucrose (wt/vol) in PBS. Coronal sections (50 μm) of the whole brain were cut using a cryostat (HM525 NX, Thermo Scientific) after being embedded with OCT compound (NEG-50, Thermo Scientific) and freezing.

Anesthesia depth measurement

EEG and EMG recordings were conducted as described previously[20]. Specifically, a stainless steel electrode was positioned over the frontal cortex for EEG measurements, while an insulated EMG electrode was inserted into the neck muscles. Additionally, a reference electrode was placed above the cerebellum. The EEG/EMG data were captured using TDT system-3 amplifiers, specifically RZ5 + RA16PA and RZ2 + PZ5 configurations. To measure the depth of anesthesia using EEG/EMG signals, a fast Fourier transform spectral analysis was employed, featuring a frequency resolution of 0.18 Hz. Data was noted every 5 seconds through a MATLAB tool and subsequently verified manually by experts. The assessment was based on

EMG power and the ratio of EEG's δ power (0.5-4Hz) to θ power (6-10Hz). EEG and EMG power values within 30 minutes post-administration were normalized to a 5-minute pre-administration baseline.

Immunohistochemistry

One out of every three brain slices (100 μm intervals) of each whole brain was washed three times with 0.1 M phosphate-buffered saline (PBS) for 10 min and permeabilized for 30 minutes at room temperature with 0.3% Triton X-100 in PBS (PBST). Slices were incubated for 2 hours at room temperature with 2% normal donkey serum (Sigma, G6767) in PBS overnight at 4°C with c-Fos primary antibodies (226003, Synaptic Systems; 1:500) diluted in PBS with 1% donkey serum. After three washes with PBST, slices were incubated with the Cy3 donkey anti-rabbit (711165152, Jackson; 1:200) secondary antibody for 2 hours at room temperature. Immunostained slices were mounted with VECTASHIELD mounting medium with DAPI and then scanned under a fluorescent microscope equipped with a 10× objective (VS120, Olympus) or a confocal microscope with a 20× objective (FV300, Olympus). Due to the limited scope of a single field of view, either 2 or 4 adjacent fields of view were stitched together to offer a comprehensive representation of specific brain regions, including the PL, ILA, LSc, LSr, SS, and VISC.

Quantification of c-Fos positive cells

The procedures used for c-Fos analysis were based on previous research [19]. A custom-written software package was employed for cellular quantification within brain images. The software consists of three components: atlas rotation, image registration, and signal detection.

Atlas rotation module

Utilizing the Allen Mouse Brain Atlas, this module allows rotations in both horizontal and vertical dimensions to align with mouse brain samples. To determine the appropriate rotation angles, we manually pinpointed anatomical landmarks corresponding to the samples. For the left-right axis rotation, we chose points from the CA3 pyramidal layer in both hemispheres and the posterior slice of the dentate gyrus, specifically the granule cell layer. For the dorsal-ventral axis rotation, we identified key anatomical landmarks. These include the initial connections of the anterior commissure and corpus callosum between the hemispheres, as well as ventral regions like the interpeduncular

nucleus and the suprachiasmatic nucleus. After determining these rotation angles, we adjusted the reference atlas to match our samples.

Image registration module

This module uses a tool that aligns brain slice images with a reference atlas, facilitating the alignment of overall brain region distribution. Registration starts by matching the coronal plane of the sample sections to the atlas. After defining the external boundaries of the brain section, the system performs geometric transformations on the section to optimize its fit with the atlas.

Signal detection module

The detection module is designed to automatically label c-Fos$^+$ cells. Post-detection, a manual verification was performed on each digitized brain section image to ensure the accuracy and precision of the c-Fos$^+$ cell markings.

Principal components analysis (PCA) of the activity patterns at whole brain

We utilized arithmetic methods to compute a logarithm ratio of the c-Fos density in a specific brain region for PCA analysis. Specifically, the cell density of a single brain region (defined as the number of c-Fos positive cells in a brain region divided by the volume of that region) was divided by the global c-Fos cell density (calculated as the total number of c-Fos positive cells throughout the entire brain divided by the total brain volume). Subsequently, the logarithm of this ratio value was taken. The formula is as follows:

$$x_R = \log 10 \left[\frac{(N_r + 1)}{V_r} \Big/ \frac{\sum_1^R (N_r + 1)}{\sum_1^R V_r} \right]$$

Nr: The number of c-Fos+ cells in each brain region. Vr: The volume of each brain region. Principal components analysis was performed on the concatenated matrix containing data from four conditions, using singular value decomposition. We then selected the first two principal components (PCs), which accounted for 56.6% of the variance in Figure 2A and 44.5% in Figure 3A.

Network generation

To evaluate how functional connectivity changed under general anesthetics in WT mice, we extracted 63 brain regions from major brain subdivisions (cerebral cortex, cerebral nuclei, thalamus, hypothalamus, midbrain, and hindbrain) listed in Supplementary Table 2. Correlation matrices were generated by computing Pearson correlation coefficients from interregional c-Fos expression in the 63 regions. Mean correlations were calculated to assess changes in functional connectivity between these major subdivisions of the brain. Weighted undirected networks were constructed by considering correlations with Pearson's r ≥0.82, corresponding to a one-tailed significance level of P<0.05 (uncorrected). The nodes in the networks represent brain regions, and the correlations that survived thresholding were considered connections. Theoretical graph analysis was performed using Brain Connectivity Toolbox (https://sites.google.com/site/bctnet/, version 2019-03-03) in MATLAB R2021 (he MathWorks Inc.) [47]. Network visualization was performed using Cytoscape (version 3.2.1) [48].

Hub identification

Network centrality was evaluated using degree, betweenness, within-module z-scores (representing within-module connectivity), and participation coefficient (indicating between-module connectivity). These measures were computed for all nodes to identify potential hub regions [49]. Modularity was assessed employing Newman's spectral community detection algorithm [50]. Degree represents the number of edges connected to a node, while betweenness denotes the number of shortest paths traversing a given node. Nodes with elevated betweenness centrality are involved in numerous shortest paths.

Statistical analysis

Sample size was determined based on prior studies [13, 14]. Data are presented as mean ± SEM, and all statistical tests were two-sided. For the c-Fos cell percentages in Figure 2C, we employed the Mann-Whitney test with a false discovery rate correction, setting a Q-value at 0.05. In Figures 4 and 5, differences in c-Fos cell counts for both KET and ISO were evaluated using an independent t-test. P-values were adjusted using the procedure by Benjamini, Krieger, and Yekutieli with Q set at 0.05 [51]. Figure 6C and Supplementary Figure 1 utilized a one-way ANOVA followed by a post-hoc

Tukey correction. Pearson correlation coefficients (R) were transformed into Z-scores using the Fisher's Z transformation before computing group means and making statistical comparisons. All statistical analyses were conducted using GraphPad Prism 9.0 (GraphPad Software, USA) and MATLAB R2021 (Mathworks Inc.). A P-value of less than 0.05 was deemed statistically significant.

Acknowledgements

We express our gratitude to our interns, Chuhang Wong from Imperial College London and Jiale Huang from ShanghaiTech University, for their assistance in cell counting.

Funding

This study was funded by the NSFC (grants 82271292, 81730031 to Y.W.; 82101350 to M.L.) and the Shanghai Municipal Key Clinical Specialty (grant shslczdzk06901 to Y.W.).

Author contributions

Yue Hu, Conceptualization, Formal analysis, Investigation, Visualization, Methodology, Writing—original draft, Writing—review and editing; Jiangtao Qi, Conceptualization, Software, Formal analysis, Investigation, Methodology, Writing—original draft, Writing—review and editing; Zhao Zhang, Resources, Investigation, Supervision, Writing—review and editing; Mengqiang Luo, Resources, Supervision, Funding acquisition, Project administration, Writing—review and editing; Yingwei Wang, Conceptualization, Resources, Supervision, Funding acquisition, Project administration, Writing—review and editing.

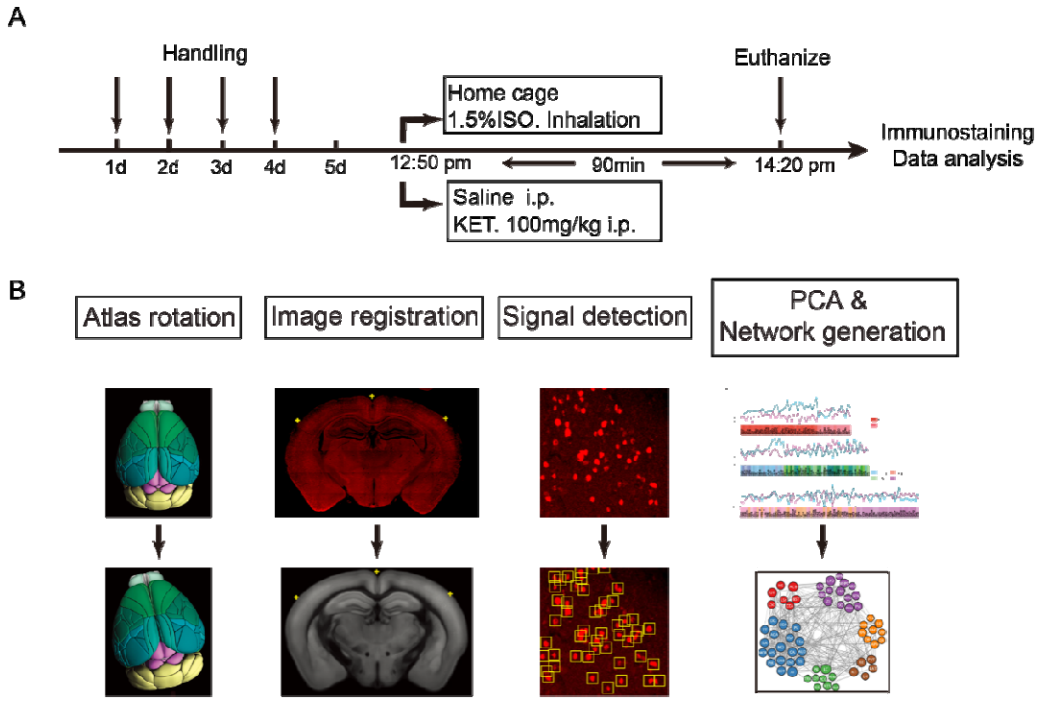

Figure 1. Brain-wide quantification of c-Fos expression.

(A) Schematic representation of the habituation protocol typically used to acclimate mice. After being exposed to anesthetics for 90 minutes, the mice were euthanized. (B) Steps for data processing. Example of brain section registration to a corresponding coronal section from the Allen Brain Atlas. For Atlas rotation, the Allen reference atlas was rotated to mimic the slice angle of the experimental brain. Image registration maps the original coronal image (upper panel) to the corresponding Allen mouse brain atlas (lower panel). The registration module applies several geometric transformations (translation, rotation, and scaling) to optimize the matching of the original image to the anatomical structures. Fluorescence signals were detected from the original image (upper panel), and once detected, they were projected onto the Allen Mouse Brain Atlas for quantification and network analysis by means of the detected signals labeled with yellow boxes.

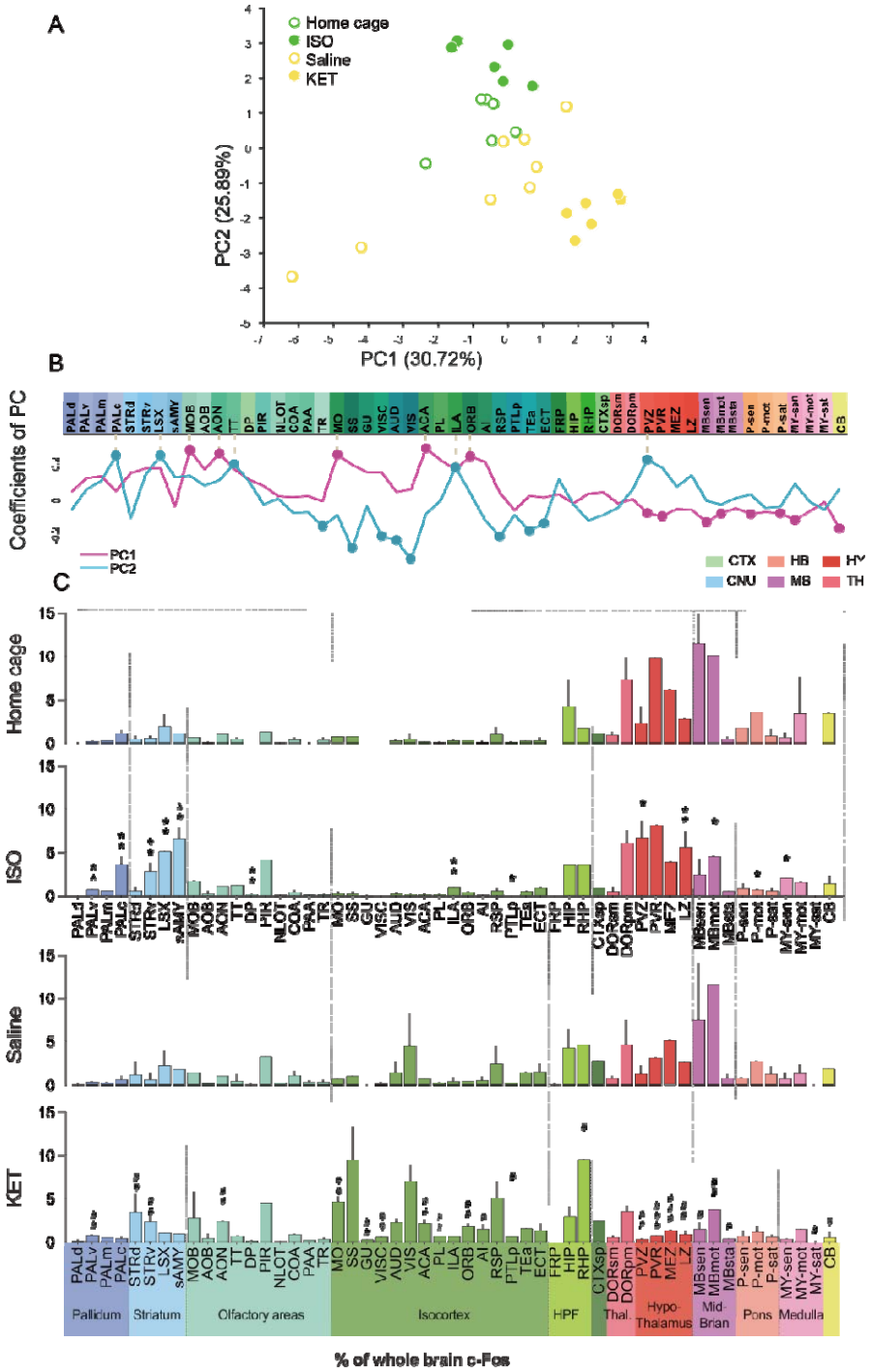

Figure 2. Whole-brain distributions of c-Fos^{+} cells induced by ISO, KET, and control conditions. (A) Scatter plot of four conditions in the space spanned by the first two principal components (PC1 versus PC2) of c-Fos density from 53 brain regions. (B) Line plot of coefficients of PC1 and PC2. Dots represent regions with absolute values larger than 75 percentiles. (C)

The normalized c-Fos^{+} cells in 53 brain areas (Home cage, n = 6; ISO, n= 6 mice; Saline, n = 8; KET, n = 6). Brain areas are grouped into 12 generalized, color-coded brain structures. Abbreviations of the 53 brain areas and percentages of c-Fos^{+} cells are listed in supplementary table 1. Error bar, mean ± SEM. Mann-Whitney tests were corrected using the false discovery rate approach with a Q-value set at 0.05. Home cage vs ISO: *P<0.05, **P<0.01, ***P<0.001. Saline vs KET: #, P<0.05, ##, P<0.01, ###, P<0.001.

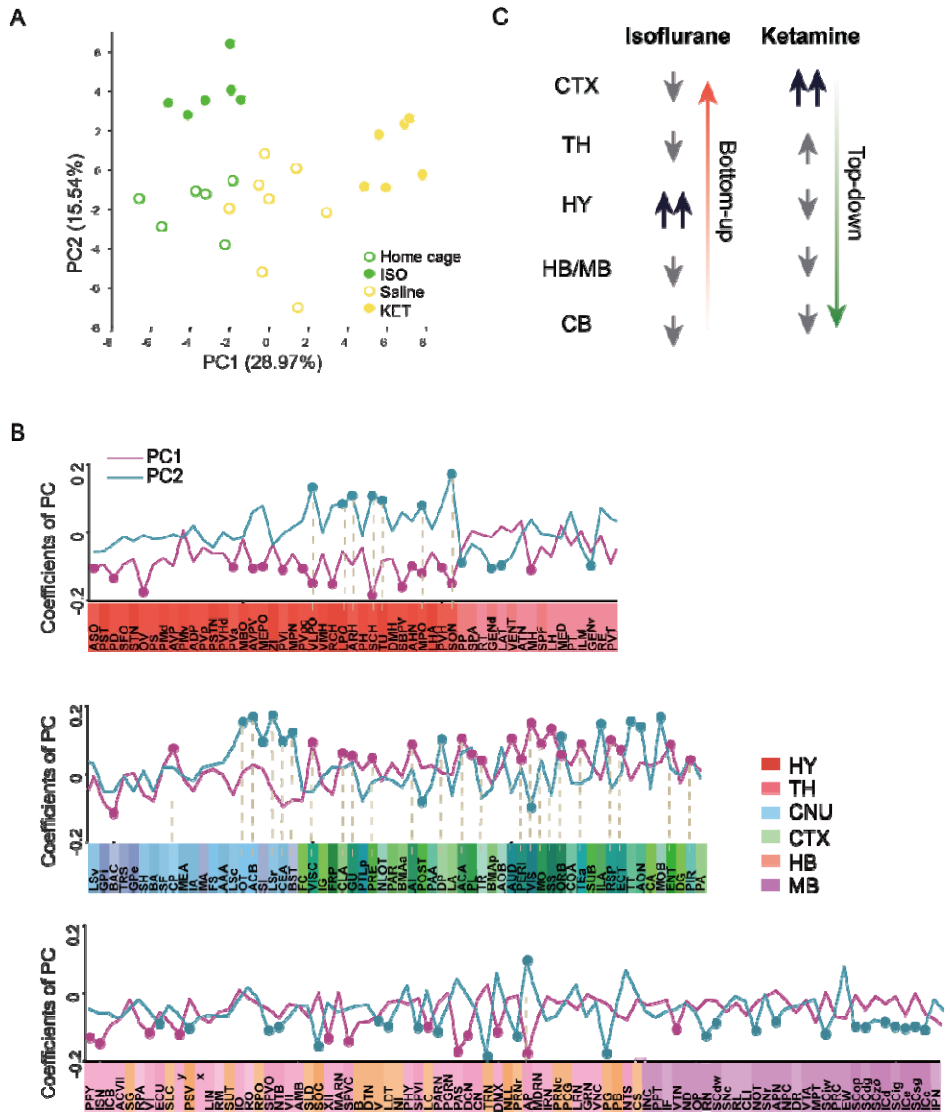

Figure 3. Similarities and differences in ISO and KET activated c-Fos brain areas. (A) Scatter plot of four conditions in the space spanned by the first two principal components (PC1 versus PC2) of normalized c-Fos density from 201 brain regions. (B) Line plot of coefficients of PC1 and PC2. Dots represent regions with absolute values larger than 75 percentiles. (C) Activation patterns of ISO and KET in different parts of brain regions were summarized. ISO was predominantly characterized by increased activation of hypothalamic and cerebral nuclei while reducing activity in the cortex and midbrain, indicating that ISO primarily exerts its effects through a bottom-up mechanism. On the other hand, KET primarily activated the cortex and inhibited hypothalamus and midbrain activity, suggesting that KET regulates consciousness through a top-down mechanism.

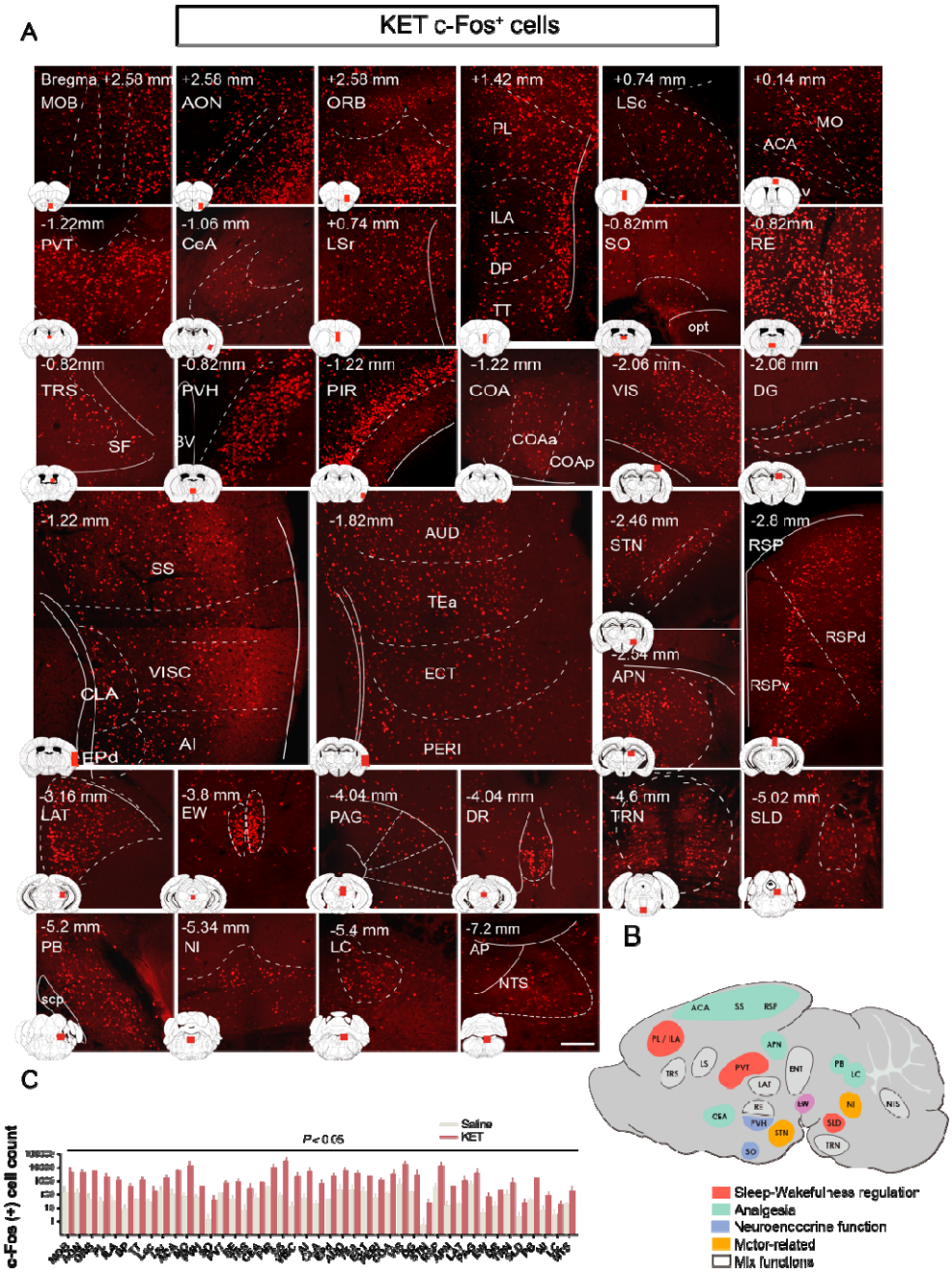

Figure 4. c-Fos expression in distinct brain regions after exposure to KET. (A) Representative immunohistochemical staining of MOB, AON, ORB, MPO, ACA, MO, TRS, PL, ILA, DP, LS, PVT, SO, PVH, RE, VISC, AI, CLA, EPd, PIR, COA, AUD, TEa, ECT, PERI, CeA, SS, DG, STN, RSP, APN, LAT, EW, DR, PAG, SLD, PB, TRN, NI, LC, NTS, and NI c-Fos^{+} cells from the indicated mice. Scale bar, 200 μm. (B) Representation of cell counts in brain

regions exhibiting significant statistical differences. Data are shown as mean ± SEM. P values < 0.05. (C) Schematic cross-section of the mouse brain showing activated brain regions by KET. Different colors indicate distinct functional nuclei. The red nuclei are associated with the regulation of sleep-wakefulness, the blue-green nuclei are linked to analgesia, the yellow nuclei are associated with motor function, and the white nuclei are a composite of various functional nuclei.

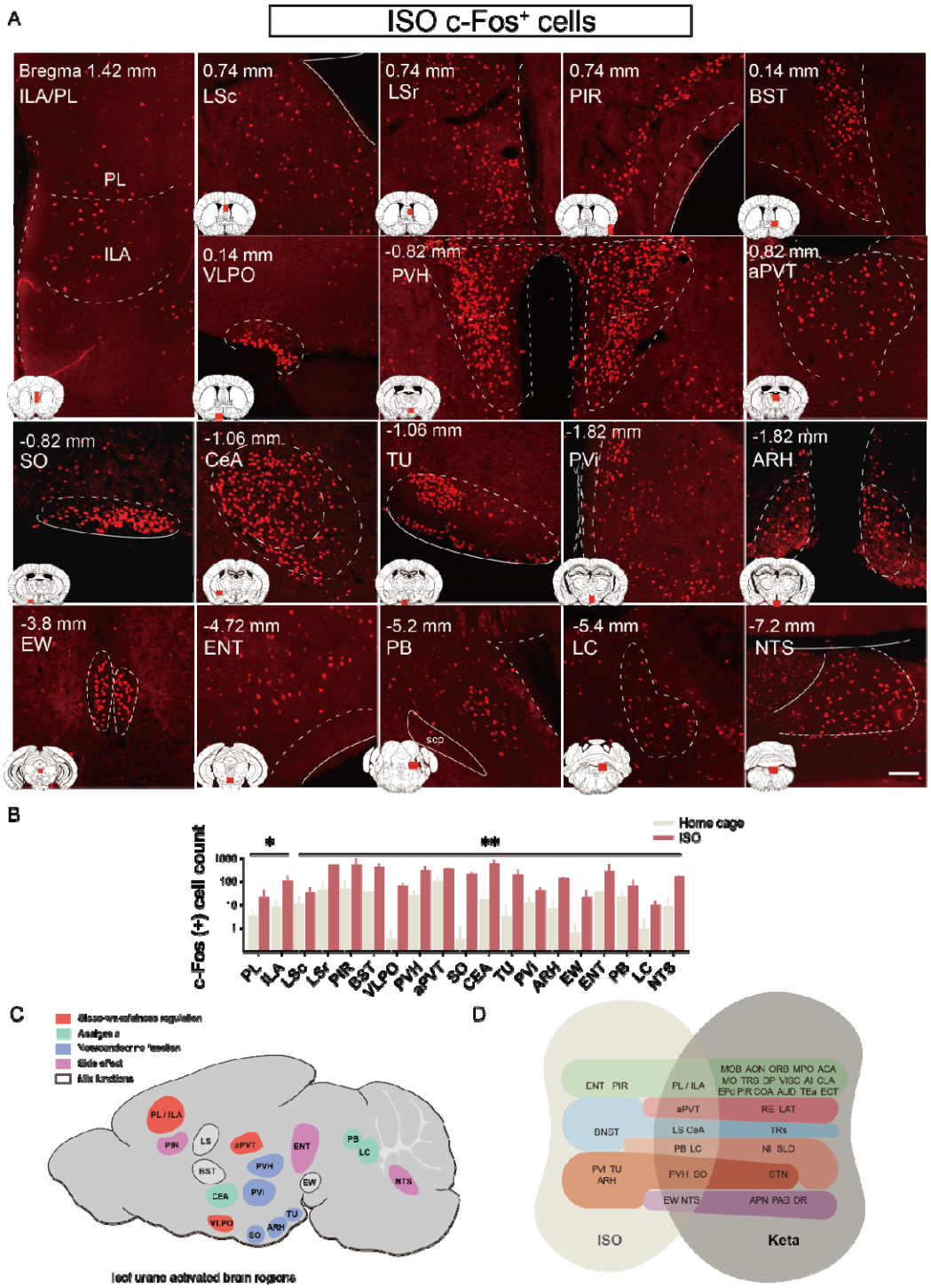

Figure 5. c-Fos expression in distinct brain regions after exposure to ISO. (A) Representative of brain regions with statistical differences c-Fos^{+} cells between the ISO group and home cage mice. Scale bar, 200 μm. (B) Representation of cell counts in brain regions exhibiting significant statistical differences between home cage and ISO. Data are shown as mean ± SEM. P

values < 0.05. (C) Schematic cross-section of the mouse brain showing activated brain regions by ISO. Different colors indicate various functionally relevant nuclei. Red signifies nuclei involved in sleep-wake regulation, blue-green in pain management, blue in neuroendocrine function, pink in side-effect management, and white denotes nuclei exhibiting mixed functionalities. (D) The Venn diagram shows brain regions that are co-activated by ISO and KET and differentially activated brain regions.

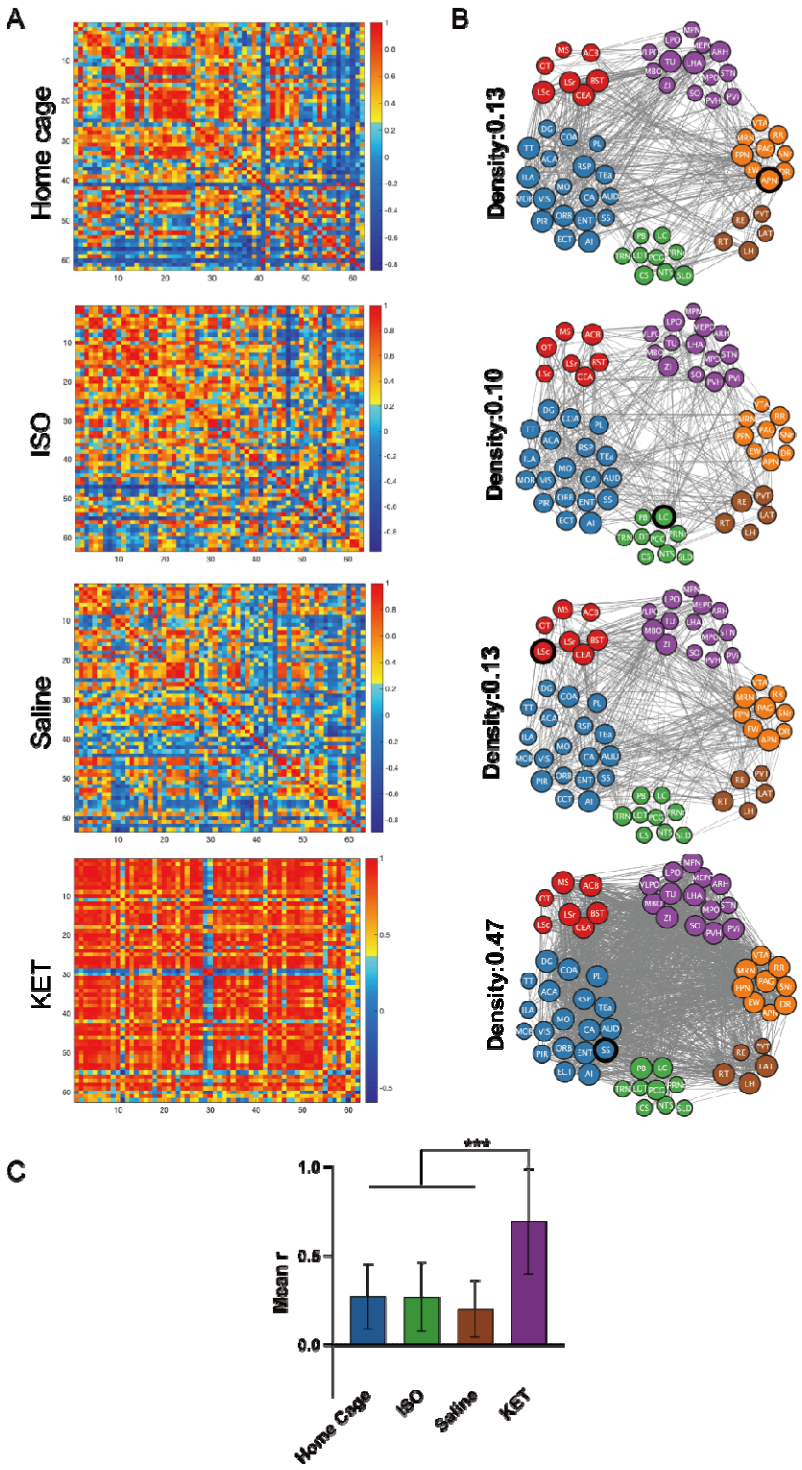

Figure 6. Generation of anesthetics-induced networks and identification of hub regions. (A) Matrices showing interregional correlations for c-Fos expression at the home cage, ISO, saline, and KET. Colors reflect correlation strength based on Pearson's r (color bar, right). Axes are numbered and

correspond to brain regions listed in Supplementary Table 5. (B) Network graphs were generated by significant positive correlations ($P < 0.05$), as well as Pearson's $r > 0.82$. The widths of the edges are proportional to the strength of the correlations and the size of the nodes is proportional to the degree of the node. Colors represent the major brain division (red, cerebral nuclei; purple, hypothalamus; orange, midbrain; brown, thalamus; blue, thalamus; green, the cerebral cortex. Network densities were noted in the left. (C) Mean r was calculated from interregional correlation coefficients. Data were analyzed using one-way ANOVA, followed by Tukey's post hoc test. ***$P < 0.001$.

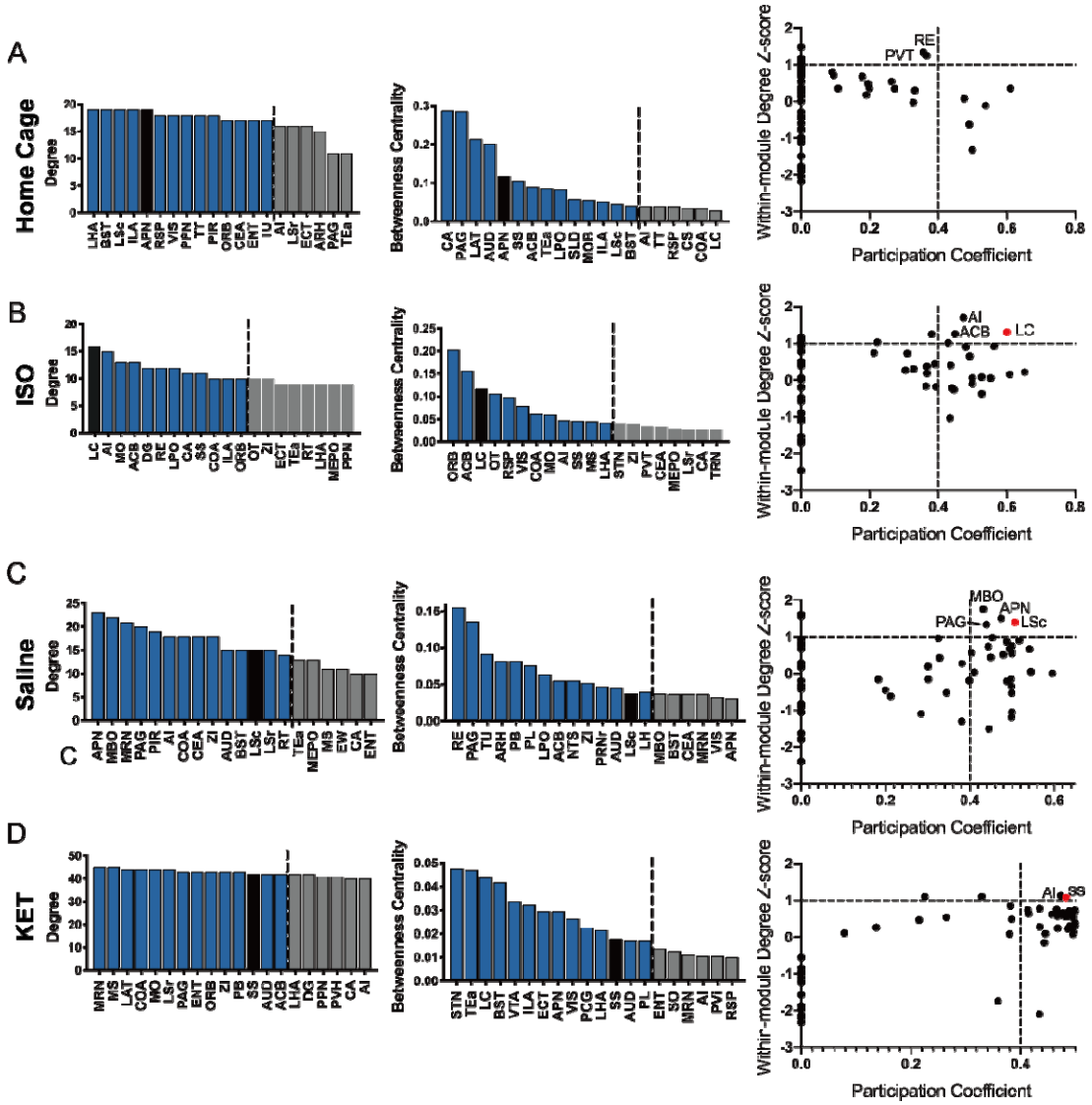

Figure 7. Identification of hub regions in the home cage (A), ISO (B), NS (C), and KET (D) groups. Each brain region is ranked in descending order based on degree and betweenness centrality, respectively. The regions to the left of the dotted line represent the top 20% in our network. Black columns highlight brain regions that rank similarly in both degree and betweenness centrality. The within-module Z-scores and participation coefficients were calculated for each brain region in the networks. Brain regions characterized by a participation coefficient greater than 0.4 and a within-module degree Z-score greater than 1 are defined as hubs and are denoted by red dots.

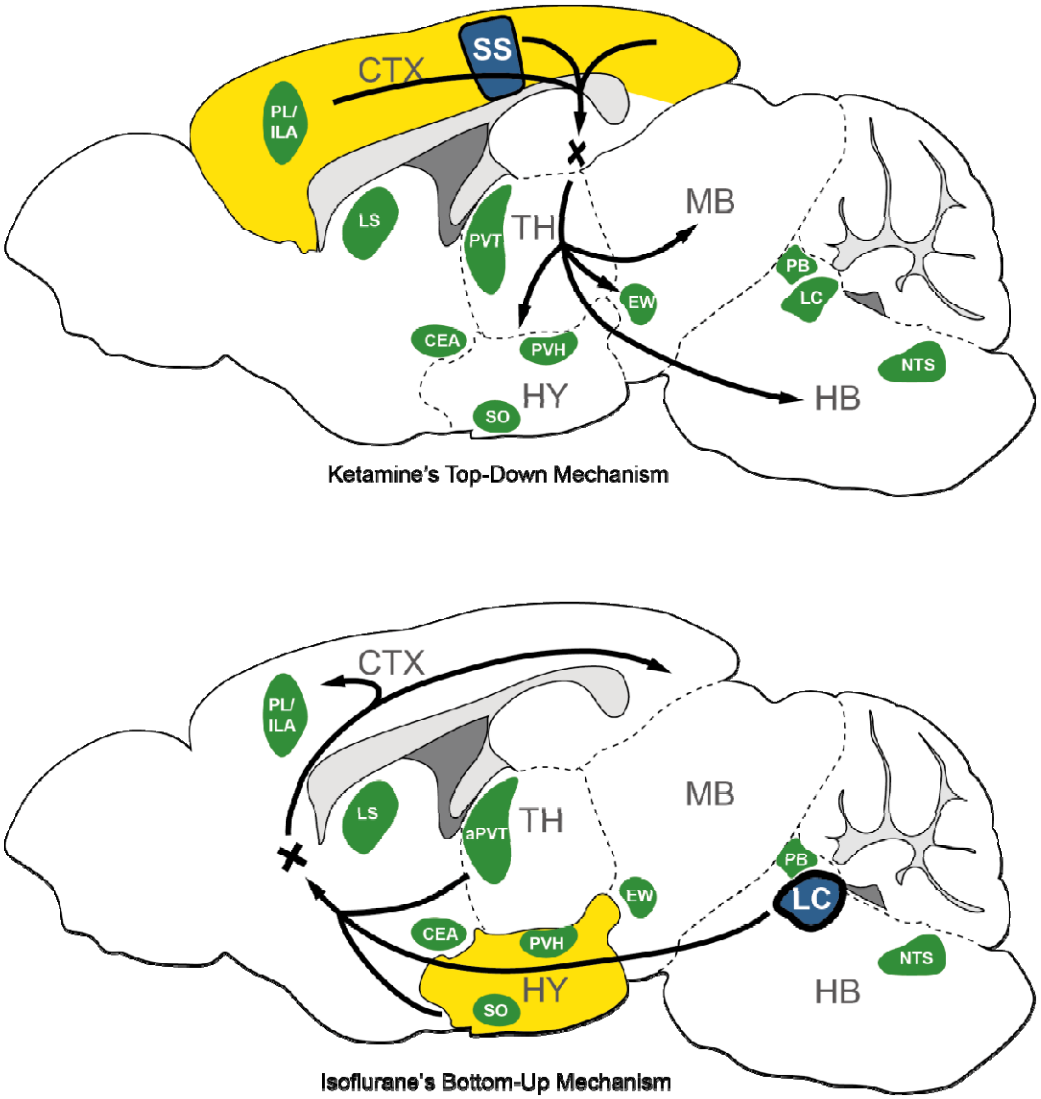

Figure 8. The possible framework for ketamine and isoflurane induced unconsciousness. The distinct pathways of ketamine and isoflurane induced unconsciousness can be explained by two contrasting mechanisms. The "top-down" process attributes KET's effect to widespread cortical activation (represented in yellow), with the somatosensory cortex (SS) acting as the central node in the functional network (depicted in blue) and relative inhibition of hypothalamic sleep-promoting nuclei. Conversely, the "bottom-up" approach posits that isoflurane induced unconsciousness arises from the activation of hypothalamic sleep-promoting regions (indicated in yellow) and relative inhibition of cortical and thalamic nuclei, with the locus coeruleus (LC) serving as the hub node in the isoflurane induced functional network. Nuclei activated by both anesthetics are shown in green. Adapted from [3, 4, 52]. PL,

prelimbic area; ILA, infralimbic areas; SON, supraoptic nucleus; PVH, paraventricular hypothalamic nucleus; TU, tuberal nucleus; LC, locus coeruleus; SS, somatosensory cortex; CTX: cortex; TH: thalamus; HY, hypothalamus; MB; midbrain; HB, hindbrain.

References

1. Hemmings HC, Jr., Riegelhaupt PM, Kelz MB, Solt K, Eckenhoff RG, Orser BA, Goldstein PA: **Towards a Comprehensive Understanding of Anesthetic Mechanisms of Action: A Decade of Discovery**. *Trends Pharmacol Sci* 2019, **40**(7):464-481.
2. Franks NP: **General anaesthesia: from molecular targets to neuronal pathways of sleep and arousal**. *Nat Rev Neurosci* 2008, **9**(5):370-386.
3. Mashour GA: **Top-down mechanisms of anesthetic-induced unconsciousness**. *Front Syst Neurosci* 2014, **8**:115.
4. Mashour GA, Hudetz AG: **Bottom-Up and Top-Down Mechanisms of General Anesthetics Modulate Different Dimensions of Consciousness**. *Front Neural Circuits* 2017, **11**:44.
5. Schroeder KE, Irwin ZT, Gaidica M, Nicole Bentley J, Patil PG, Mashour GA, Chestek CA: **Disruption of corticocortical information transfer during ketamine anesthesia in the primate brain**. *NeuroImage* 2016, **134**:459-465.
6. Lee U, Ku S, Noh G, Baek S, Choi B, Mashour GA: **Disruption of frontal-parietal communication by ketamine, propofol, and sevoflurane**. *Anesthesiology* 2013, **118**(6):1264-1275.
7. Moore JT, Chen J, Han B, Meng QC, Veasey SC, Beck SG, Kelz MB: **Direct Activation of Sleep-Promoting VLPO Neurons by Volatile Anesthetics Contributes to Anesthetic Hypnosis**. *Curr Biol* 2012, **22**(21):2008-2016.
8. Nelson LE, Guo TZ, Lu J, Saper CB, Franks NP, Maze M: **The sedative component of anesthesia is mediated by GABA(A) receptors in an endogenous sleep pathway**. *Nat Neurosci* 2002, **5**(10):979-984.
9. Yap EL, Greenberg ME: **Activity-Regulated Transcription: Bridging the Gap between Neural Activity and Behavior**. *Neuron* 2018, **100**(2):330-348.
10. Morgan JI, Curran T: **Stimulus-transcription coupling in neurons: role of cellular immediate-early genes**. *Trends Neurosci* 1989, **12**(11):459-462.
11. Zhang D, Liu J, Zhu T, Zhou C: **Identifying c-fos Expression as a Strategy to Investigate the Actions of General Anesthetics on the Central Nervous System**. *Curr Neuropharmacol* 2022, **20**(1):55-71.
12. Smith ML, Li J, Cote DM, Ryabinin AE: **Effects of isoflurane and ethanol administration on c-Fos immunoreactivity in mice**. *Neuroscience* 2016, **316**:337-343.
13. Lu J, Nelson LE, Franks N, Maze M, Chamberlin NL, Saper CB: **Role of endogenous sleep-wake and analgesic systems in anesthesia**. *J Comp Neurol* 2008, **508**(4):648-662.
14. Yatziv SL, Yudco O, Dickmann S, Devor M: **Patterns of neural activity in the mouse brain: Wakefulness vs. General anesthesia**. *Neurosci Lett* 2020, **735**:135212.
15. Han B, McCarren HS, O'Neill D, Kelz MB: **Distinctive recruitment of endogenous sleep-promoting neurons by volatile anesthetics and a nonimmobilizer**. *Anesthesiology* 2014,

121(5):999-1009.

16. Gelegen C, Miracca G, Ran MZ, Harding EC, Ye Z, Yu X, Tossell K, Houston CM, Yustos R, Hawkins ED *et al*: **Excitatory Pathways from the Lateral Habenula Enable Propofol-Induced Sedation**. *Curr Biol* 2018, **28**(4):580-587.e585.
17. Hua T, Chen B, Lu D, Sakurai K, Zhao S, Han BX, Kim J, Yin L, Chen Y, Lu J *et al*: **General anesthetics activate a potent central pain-suppression circuit in the amygdala**. *Nat Neurosci* 2020, **23**(7):854-868.
18. Jiang-Xie LF, Yin L, Zhao S, Prevosto V, Han BX, Dzirasa K, Wang F: **A Common Neuroendocrine Substrate for Diverse General Anesthetics and Sleep**. *Neuron* 2019, **102**(5):1053-1065.e1054.
19. Ma G, Liu Y, Wang L, Xiao Z, Song K, Wang Y, Peng W, Liu X, Wang Z, Jin S: **Hierarchy in sensory processing reflected by innervation balance on cortical interneurons**. *Science Advances* 2021, **7**(20):eabf5676.
20. Luo M, Fei X, Liu X, Jin Z, Wang Y, Xu M: **Divergent Neural Activity in the VLPO During Anesthesia and Sleep**. *Adv Sci (Weinh)* 2023, **10**(2):e2203395.
21. Do JP, Xu M, Lee SH, Chang WC, Zhang S, Chung S, Yung TJ, Fan JL, Miyamichi K, Luo L *et al*: **Cell type-specific long-range connections of basal forebrain circuit**. *Elife* 2016, **5**.
22. Mashour GA, Pal D, Brown EN: **Prefrontal cortex as a key node in arousal circuitry**. *Trends Neurosci* 2022, **45**(10):722-732.
23. Gao C, Leng Y, Ma J, Rooke V, Rodriguez-Gonzalez S, Ramakrishnan C, Deisseroth K, Penzo MA: **Two genetically, anatomically and functionally distinct cell types segregate across anteroposterior axis of paraventricular thalamus**. *Nat Neurosci* 2020, **23**(2):217-228.
24. Cho JR, Treweek JB, Robinson JE, Xiao C, Bremner LR, Greenbaum A, Gradinaru V: **Dorsal Raphe Dopamine Neurons Modulate Arousal and Promote Wakefulness by Salient Stimuli**. *Neuron* 2017, **94**(6):1205-1219.e1208.
25. Feng H, Wen SY, Qiao QC, Pang YJ, Wang SY, Li HY, Cai J, Zhang KX, Chen J, Hu ZA *et al*: **Orexin signaling modulates synchronized excitation in the sublaterodorsal tegmental nucleus to stabilize REM sleep**. *Nat Commun* 2020, **11**(1):3661.
26. Bliss TV, Collingridge GL, Kaang BK, Zhuo M: **Synaptic plasticity in the anterior cingulate cortex in acute and chronic pain**. *Nat Rev Neurosci* 2016, **17**(8):485-496.
27. Villarreal CF, Del Bel EA, Prado WA: **Involvement of the anterior pretectal nucleus in the control of persistent pain: a behavioral and c-Fos expression study in the rat**. *Pain* 2003, **103**(1-2):163-174.
28. Cheriyan J, Sheets PL: **Altered Excitability and Local Connectivity of mPFC-PAG Neurons in a Mouse Model of Neuropathic Pain**. *J Neurosci* 2018, **38**(20):4829-4839.
29. Yeung JC, Yaksh TL, Rudy TA: **Concurrent mapping of brain sites for sensitivity to the direct application of morphine and focal electrical stimulation in the production of antinociception in the rat**. *Pain* 1977, **4**(1):23-40.
30. Llorca-Torralba M, Camarena-Delgado C, Suárez-Pereira I, Bravo L, Mariscal P, Garcia-Partida JA, López-Martín C, Wei H, Pertovaara A, Mico JA *et al*: **Pain and depression comorbidity causes asymmetric plasticity in the locus coeruleus neurons**. *Brain* 2021, **145**(1):154-167.

31. Duncan GE, Moy SS, Knapp DJ, Mueller RA, Breese GR: **Metabolic mapping of the rat brain after subanesthetic doses of ketamine: potential relevance to schizophrenia**. *Brain Res* 1998, **787**(2):181-190.
32. Ma S, Allocca G, Ong-Pålsson EK, Singleton CE, Hawkes D, McDougall SJ, Williams SJ, Bathgate RA, Gundlach AL: **Nucleus incertus promotes cortical desynchronization and behavioral arousal**. *Brain Struct Funct* 2017, **222**(1):515-537.
33. Musacchio T, Rebenstorff M, Fluri F, Brotchie JM, Volkmann J, Koprich JB, Ip CW: **Subthalamic nucleus deep brain stimulation is neuroprotective in the A53T α-synuclein Parkinson's disease rat model**. *Ann Neurol* 2017, **81**(6):825-836.
34. Hauer BE, Pagliardini S, Dickson CT: **Prefrontal-Hippocampal Pathways Through the Nucleus Reuniens Are Functionally Biased by Brain State**. *Front Neuroanat* 2021, **15**:804872.
35. Deng J, Zhou H, Lin JK, Shen ZX, Chen WZ, Wang LH, Li Q, Mu D, Wei YC, Xu XH *et al*: **The Parabrachial Nucleus Directly Channels Spinal Nociceptive Signals to the Intralaminar Thalamic Nuclei, but Not the Amygdala**. *Neuron* 2020, **107**(5):909-923 e906.
36. Bekkers JM, Suzuki N: **Neurons and circuits for odor processing in the piriform cortex**. *Trends Neurosci* 2013, **36**(7):429-438.
37. Xu W, Wilson DA: **Odor-evoked activity in the mouse lateral entorhinal cortex**. *Neuroscience* 2012, **223**:12-20.
38. Gupta RG, Schafer C, Ramaroson Y, Sciullo MG, Horn CC: **Role of the abdominal vagus and hindbrain in inhalational anesthesia-induced vomiting**. *Auton Neurosci* 2017, **202**:114-121.
39. Yi T, Wang N, Huang J, Wang Y, Ren S, Hu Y, Xia J, Liao Y, Li X, Luo F *et al*: **A Sleep-Specific Midbrain Target for Sevoflurane Anesthesia**. *Adv Sci (Weinh)* 2023:e2300189.
40. Wheeler AL, Teixeira CM, Wang AH, Xiong X, Kovacevic N, Lerch JP, McIntosh AR, Parkinson J, Frankland PW: **Identification of a functional connectome for long-term fear memory in mice**. *PLoS Comput Biol* 2013, **9**(1):e1002853.
41. Leung LS, Luo T, Ma J, Herrick I: **Brain areas that influence general anesthesia**. *Prog Neurobiol* 2014, **122**:24-44.
42. Power JD, Schlaggar BL, Lessov-Schlaggar CN, Petersen SE: **Evidence for hubs in human functional brain networks**. *Neuron* 2013, **79**(4):798-813.
43. Meunier D, Achard S, Morcom A, Bullmore E: **Age-related changes in modular organization of human brain functional networks**. *NeuroImage* 2009, **44**(3):715-723.
44. Zerbi V, Floriou-Servou A, Markicevic M, Vermeiren Y, Sturman O, Privitera M, von Ziegler L, Ferrari KD, Weber B, De Deyn PP *et al*: **Rapid Reconfiguration of the Functional Connectome after Chemogenetic Locus Coeruleus Activation**. *Neuron* 2019, **103**(4):702-718 e705.
45. Vierck CJ, Whitsel BL, Favorov OV, Brown AW, Tommerdahl M: **Role of primary somatosensory cortex in the coding of pain**. *Pain* 2013, **154**(3):334-344.
46. Cichon J, Wasilczuk AZ, Looger LL, Contreras D, Kelz MB, Proekt A: **Ketamine triggers a switch in excitatory neuronal activity across neocortex**. *Nat Neurosci* 2023, **26**(1):39-52.
47. Rubinov M, Sporns O: **Complex network measures of brain connectivity: uses and interpretations**. *NeuroImage* 2010, **52**(3):1059-1069.
48. Shannon P, Markiel A, Ozier O, Baliga NS, Wang JT, Ramage D, Amin N, Schwikowski B, Ideker T: **Cytoscape: a software environment for integrated models of biomolecular interaction**

networks. *Genome Res* 2003, **13**(11):2498-2504.

49. Guimera R, Nunes Amaral LA: **Functional cartography of complex metabolic networks**. *Nature* 2005, **433**(7028):895-900.

50. Newman ME: **Modularity and community structure in networks**. *Proceedings of the National Academy of Sciences of the United States of America* 2006, **103**(23):8577-8582.

51. Benjamini Y, Hochberg Y: **Controlling the false discovery rate: a practical and powerful approach to multiple testing**. *Journal of the Royal statistical society: series B (Methodological)* 1995, **57**(1):289-300.

52. Reimann HM, Niendorf T: **The (Un)Conscious Mouse as a Model for Human Brain Functions: Key Principles of Anesthesia and Their Impact on Translational Neuroimaging**. *Front Syst Neurosci* 2020, **14**:8.

53. Nagata A, Nakao S, Miyamoto E, Inada T, Tooyama I, Kimura H, Shingu K: **Propofol inhibits ketamine-induced c-fos expression in the rat posterior cingulate cortex**. *Anesth Analg* 1998, **87**(6):1416-1420.

54. Nagata A, Nakao Si S, Nishizawa N, Masuzawa M, Inada T, Murao K, Miyamoto E, Shingu K: **Xenon inhibits but N(2)O enhances ketamine-induced c-Fos expression in the rat posterior cingulate and retrosplenial cortices**. *Anesth Analg* 2001, **92**(2):362-368.

55. Inta D, Trusel M, Riva MA, Sprengel R, Gass P: **Differential c-Fos induction by different NMDA receptor antagonists with antidepressant efficacy: potential clinical implications**. *Int J Neuropsychopharmacol* 2009, **12**(8):1133-1136.

56. Nakao S, Arai T, Mori K, Yasuhara O, Tooyama I, Kimura H: **High-dose ketamine does not induce c-Fos protein expression in rat hippocampus**. *Neurosci Lett* 1993, **151**(1):33-36.

57. Nakao S, Miyamoto E, Masuzawa M, Kambara T, Shingu K: **Ketamine-induced c-Fos expression in the mouse posterior cingulate and retrosplenial cortices is mediated not only via NMDA receptors but also via sigma receptors**. *Brain Res* 2002, **926**(1-2):191-196.

58. Hase T, Hashimoto T, Saito H, Uchida Y, Kato R, Tsuruga K, Takita K, Morimoto Y: **Isoflurane induces c-Fos expression in the area postrema of the rat**. *Journal of anesthesia* 2019, **33**(4):562-566.

Supplementary Information

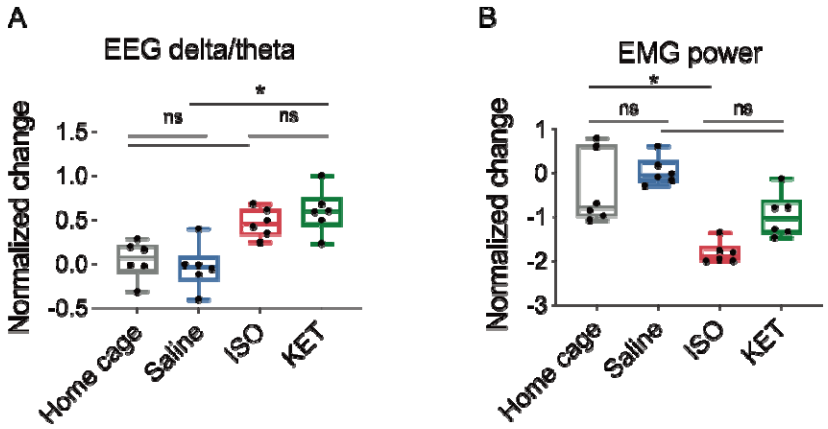

Supplementary Figure 1. EEG and EMG power change after each treatment. Box represents the 25th-75th percentiles; the central line denotes the median; whiskers indicate maximum and minimum values. n = 6, 6, 6, 6 for the home cage, ISO, saline, and KET, respectively. (A) Normalized Change in EEG power: ISO vs KET, P > 0.99; Saline vs KET, P = 0.01; Home cage vs ISO, P = 0.11. (B) Normalized Change in EMG power: ISO vs KET, P = 0.36; Saline vs KET, P = 0.30; Home cage vs ISO, P = 0.02. Analyses were conducted using the Kruskal-Wallis test, followed by Dunn's multiple comparisons test.

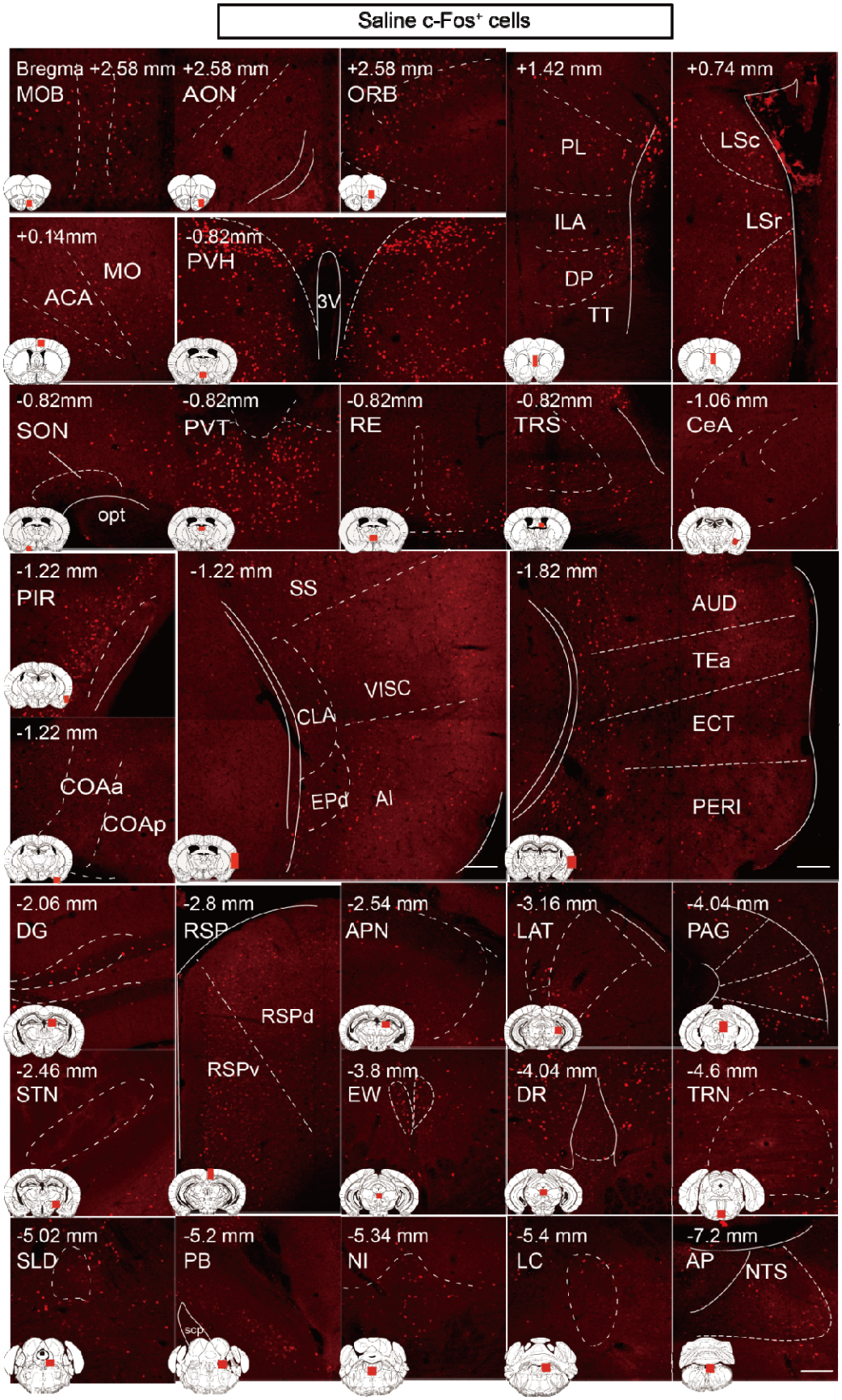
Saline c-Fos⁺ cells
Bregma +2.58 mm
MOB
+2.58 mm
AON
+2.58 mm
ORB
+1.42 mm
PL
ILA
DP
TT
+0.74 mm
LSc
LSr
+0.14mm
MO
ACA
-0.82mm
PVH
3V
-0.82mm
SON
opt
-0.82mm
PVT
-0.82mm
RE
-0.82mm
TRS
-1.06 mm
CeA
-1.22 mm
PIR
-1.22 mm
COAa
COAp
-1.22 mm
SS
VISC
CLA
EPd
AI
-1.82 mm
AUD
TEa
ECT
PERI
-2.06 mm
DG
-2.8 mm
RSP
RSPd
RSPv
-2.54 mm
APN
-3.16 mm
LAT
-4.04 mm
PAG
-2.46 mm
STN
-3.8 mm
EW
-4.04 mm
DR
-4.6 mm
TRN
-5.02 mm
SLD
-5.2 mm
PB
scp
-5.34 mm
NI
-5.4 mm
LC
-7.2 mm
AP
NTS

867

Supplementary Figure 2. c-Fos expression in distinct brain regions after exposure to normal saline administration. (A) Representative immunohistochemical staining of MOB, AON, ORB, MPO, ACA, MO, TRS, PL, ILA, DP, LS, PVT, SON, PVH, RE, VISC, AI, CLA, EPd, PIR, COA, AUD, TEa, ECT, PERI, CeA, SS, DG, STN, RSP, APN, LAT, EW, DR, PAG, SLD, PB, TRN, NI, LC, and NTS c-Fos^{+} cells from the indicated mice. Scale bar, 200 μm.

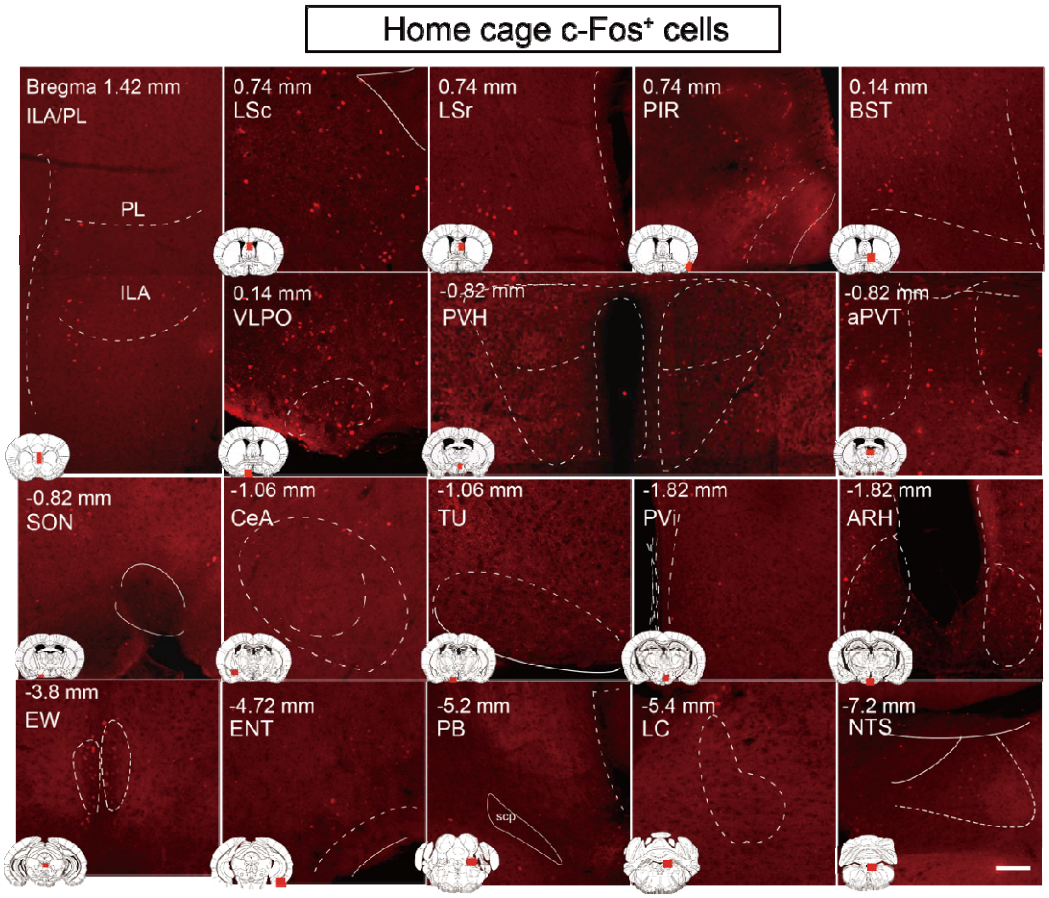

Supplementary Figure 3. c-Fos expression in home cage group. (A) Representative immunohistochemical staining of PL, ILA, LSc, LSr, PIR, BST, VLPO, PVH, aPVT, SON, CeA, TU, PVi, ARH, EW, ENT, PB, LC, and NTS c-Fos^{+} cells from the indicated mice. Scale bar, 200 μm.

Supplementary Table 1: c-Fos-positive cell counts in each brain region normalized to the total cell count of their respective whole brains for the home Cage, ISO, saline, and KET groups. P1 denotes p-values for comparisons between the Home Cage and ISO groups, while P2 represents p-values for the contrasts between the Saline and KET groups. Statistical evaluations were undertaken using the Mann-Whitney test, followed by a false discovery rate (FDR) correction, with a threshold Q-value established at 0.05.

Brain Structure	Substructure	Abbreviation	Home cage	ISO	*P* 1	Saline	KET	*P* 2
Pallidum	Pallidum,dorsal region	PALd	0.057± 0.028	0.010± 0.005	0.275	0.080± 0.048	0.131± 0.065	0.179
	Pallidum,ventral region	PALv	0.253± 0.083	0.712± 0.093	0.009	0.363± 0.157	0.785± 0.106	0.020
	Pallidum,medial region	PALm	0.311± 0.096	0.575± 0.054	0.065	0.305± 0.080	0.511± 0.060	0.081
	Pallidum,caudal region	PALc	1.108± 0.184	3.648± 0.356	0.002	0.626± 0.186	0.402± 0.107	0.852
Striatum	Striatum dorsal region	STRd	0.500± 0.126	0.572± 0.183	0.937	1.191± 0.543	3.466± 0.840	0.013
	Striatum ventral region	STRv	0.589± 0.098	2.774± 0.402	0.002	0.597± 0.267	2.312± 0.287	0.005
	Lateral septal complex	LSX	1.932± 0.586	5.108± 0.413	0.004	2.285± 0.610	1.052± 0.059	0.135
	Striatum-like amygdalar nuclei	sAMY	1.135± 0.376	6.541± 0.541	0.002	1.830± 0.417	0.952± 0.283	0.142
Olfactory areas	Main olfactory bulb	MOB	0.677± 0.292	1.702± 0.517	0.177	1.420± 0.791	2.792± 1.255	0.217
	Accessory olfactory bulb	AOB	0.109± 0.066	0.208± 0.139	0.697	0.178± 0.093	0.419± 0.228	0.225
	Anterior olfactory nucleus	AON	0.999± 0.548	1.117± 0.354	0.485	1.053± 0.486	2.376± 0.681	0.041
	Taenia tecta	TT	0.469± 0.099	1.193± 0.274	0.093	0.463± 0.280	0.700± 0.254	0.172
	Dorsal peduncular area	DP	0.020± 0.009	0.171± 0.047	0.002	0.075± 0.035	0.162± 0.044	0.103
	Piriform area	PIR	1.300± 0.356	4.166± 1.449	0.093	3.248± 0.528	4.515± 0.747	0.282

	Nucleus of the lateral olfactory tract	NLOT	0.097± 0.044	0.091± 0.040	0.699	0.240± 0.120	0.090± 0.029	0.414
	Cortical amygdalar area	COA	0.365± 0.114	0.430± 0.096	0.589	1.140± 0.193	0.878± 0.210	0.662
	Piriform-amygdalar area	PAA	0.063± 0.018	0.120± 0.040	0.329	0.336± 0.076	0.213± 0.049	0.345
	Post piriform transition area	TR	0.324± 0.131	0.130± 0.058	0.387	0.350± 0.089	0.325± 0.072	>0.999999
Isocortex	*Somatomotor areas*	*MO*	*0.736± 0.225*	*0.263± 0.105*	0.093	0.715± 0.225	4.671± 0.244	0.001
	Somatosensory areas	SS	0.775± 0.309	0.231± 0.123	0.093	1.058± 0.489	9.487± 1.551	0.001
	Gustatory areas	GU	0.032± 0.019	0.048± 0.018	0.387	0.040± 0.017	0.288± 0.044	0.001
	Visceral area	VISC	0.014± 0.007	0.004± 0.003	0.318	0.147± 0.071	0.564± 0.142	0.029
	Auditory areas	AUD	0.256± 0.093	0.246± 0.081	>0.999999	1.481± 0.427	2.267± 0.198	0.142
	Visual areas	VIS	0.501± 0.247	0.189± 0.044	0.818	4.503± 1.343	7.013± 0.775	0.181
	Anterior cingulate area	ACA	0.183± 0.078	0.146± 0.037	0.981	0.736± 0.337	2.179± 0.145	0.020
	Prelimbic area	PL	0.118± 0.043	0.160± 0.053	0.485	0.283± 0.100	0.649± 0.086	0.028
	Infralimbic area	ILA	0.279± 0.056	0.922± 0.144	0.002	0.409± 0.182	0.615± 0.217	0.393
	Orbital area	ORB	0.337± 0.083	0.393± 0.054	0.485	0.453± 0.167	1.759± 0.152	0.001
	Agranular insular area	AI	0.146± 0.047	0.096± 0.032	0.485	0.533± 0.164	1.475± 0.231	0.013
	Retrosplenial area	RSP	1.007± 0.349	0.552± 0.114	0.394	2.455± 0.721	5.070± 0.773	0.043
	Posterior parietal association areas	PTLp	0.149± 0.032	0.035± 0.016	0.041	0.238± 0.111	0.598± 0.359	0.634
	Temporal association areas	TEa	0.266± 0.104	0.513± 0.194	0.310	1.501± 0.433	1.539± 0.135	0.573
	Ectorhinal area	ECT	0.305± 0.144	0.901± 0.384	0.169	1.507± 0.341	1.301± 0.341	0.755
	Frontal Pole, cerebral cortex	FRP	0.020± 0.013	0.030± 0.027	>0.999999	0.074± 0.043	0.029± 0.012	0.750
Hippocamp	Hippocampal	HIP	4.240±	3.531±	0.699	4.281±	2.938±	0.228

al formation	region		1.230	0.843		0.766	0.469	
	Retrohippocampal region	RHP	1.689± 0.500	3.558± 1.068	0.132	4.627± 1.113	9.551± 0.967	0.013
Cortical subplate	Cortical subplate	CTXsp	1.122± 0.216	0.910± 0.181	0.589	2.798± 0.440	2.410± 0.226	0.662
Thalamus	Thalamus, sensory motor cortex-related	DORsm	0.881± 0.160	0.505± 0.185	0.132	0.779± 0.102	0.546± 0.082	0.181
	Thalamus, polymodal association cortex-related	DORpm	7.353± 1.042	6.104± 0.601	0.180	4.674± 0.992	3.502± 0.259	0.662
Hypothalamus	Periventricular zone	PVZ	2.330± 0.759	6.627± 0.843	0.015	1.306± 0.345	0.334± 0.068	0.008
	Periventricular region	PVR	9.800± 2.909	8.145± 0.869	0.937	3.140± 0.421	0.762± 0.088	0.001
	Hypothalamic medial zone	MEZ	6.198± 1.192	3.878± 0.204	0.240	5.121± 0.832	1.349± 0.174	0.001
	Hypothalamic lateral zone	LZ	2.815± 0.304	5.589± 0.752	0.002	2.606± 0.718	0.883± 0.167	0.005
Midbrain	Midbrain, sensory-related	MBsen	11.525 ±3.354	2.449± 0.735	0.065	7.507± 2.343	1.466± 0.332	0.020
	Midbrain, motor-related	MBmot	10.099 ±1.299	4.515± 1.105	0.041	11.659 ±1.716	3.712± 0.588	0.005
	Midbrain, behavioral state-related	MBsta	0.471± 0.125	0.535± 0.145	0.699	0.834± 0.168	0.380± 0.099	0.043
Pons	Pons, sensory-related	P-sen	1.729± 0.917	0.806± 0.261	0.937	0.842± 0.149	0.661± 0.231	0.573
	Pons, motor-related	P-mot	3.579± 1.115	0.715± 0.197	0.015	2.772± 0.562	1.168± 0.247	0.081
	Pons, behavioral state-related	P-sat	0.816± 0.314	0.572± 0.115	0.818	1.286± 0.308	0.564± 0.109	0.059
Medulla	Medulla, sensory-related	MY-sen	0.618± 0.241	2.042± 0.426	0.015	0.700± 0.249	0.356± 0.098	0.345
	Medulla, motor-related	MY-mot	3.410± 1.727	1.542± 0.144	>0.999999	1.347± 0.369	1.476± 0.374	0.852
	Medulla, behavioral state-related	MY-sat	0.020± 0.013	0.019± 0.008	0.740	0.024± 0.011	0.078± 0.032	0.043
Cerebellu	Cerebellum	CB	3.451±	1.379±	0.310	1.869±	0.508±	0.020

m	1.469	0.352	0.611	0.245

Shown are the mean ± SEM. of the percentage of c-Fos^{+} cells in each area.

Supplementary Table 2. Sum of previous studies on ketamine activated brain regions detected by c-Fos immunostaining.

Brain regions	Function	Treatment Regimen	Duration	Time of day	Effect	References
CeA	Pain Suppression	100mg/kg and 10mg/kgxylazine i.p.	2h	/	Up-regulated	Hua T, et al.,(2022) [17]
SON	Natural sleep/General anesthesia	100mg/kg with or without xylazine(10mg/kg) i.p	2h	/	Up-regulated	Jiang-Xie LF, et al.,(2019) [18]
pCC	/	100mg/kg i.p.	2h	/	Up-regulated	Nagata A, et al.,(1998) [53]
pCC, RSC	/	100mg/kg i.p.	2h	/	Up-regulated	Nagata A, et al.,(2001) [54]
RSP, CeA, Midline thalamic nuclei	Antidepressant	10mg/kg i.p.	1.5h	/	Up-regulated	Inta D, et al.,(2009) [55]
Cg, BF, Orx, TMN, vlPAG, LC, LHb, EW, midline thalamus	LC/vPAG engaged in analgesia	150mg/kg, 60mg/kg, 30mg/kg i.p.	2h	ZT3	Up-regulated	Lu J, et al.,(2008) [13]
CC, PVT	/	100mg/kg i.p.	/	/	/	Nakao S, et al.,(1993) [56]
PC, RSP	/	50mg/kg i.p.	2h	ZT3-9	Up-regulated	Nakao S, et al.,(2002) [57]

Abbreviation: CeA, Central amygdalar nucleus; SON, Supraoptic nucleus; pCC, Posterior cingulate cortex; RSC, Retrosplenial cortex; RSP, Retrosplenial area; Cg, cingulate cortex; BF, basal forebrain cholinergic cells; Orx, perifornical orexin cells; vlPAG, ventrolateral periaquductal gray

dopamine cells; LC, Locus coeruleus; LHb, lateral habenular nucleus; EW, Edinger-Westphal nucleus; CC, Cerebral cortex; PVT, Paraventricular nucleus of the thalamus; PC, posterior cingulate. RSP, Retrosplenial area.

Supplementary Table 3. The sum of previous studies on isoflurane activated brain regions detected by c-Fos immunostaining.

Brain regions	Function	Concentration of ISO	Duration	Time of day		References
VLPO	Sleep-Promoting, Hypnosis	1.2%, 0.6%, 0.3%	2h	ZT12-14/ZT4-6	Up-regulated	Moore JT,.et al.,(2012) [7]
PIR, LSD, LSV	/	4% 5mins+1%	2h	ZT2-7	Up-regulated	Smith ML, et al.,(2016) [12]
NTS, VeN	Vomiting	1% and 3%	1.5h	/	Up-regulated	Gupta RG, et al.,(2016) [38]
CeA	Pain Suppression	1.5%	2h	/	Up-regulated	Hua T, et al.,(2022) [17]
SON	Natural sleep, General anesthesia	1%,1.2%	2h	/	Up-regulated	Jiang-Xie LF, et al.,(2019) [18]
VLPO, MnPO	Sleep and unconsciousness	1.2%	2h	ZT14-17	Up-regulated	Han B, et al.,(2022) [15]
EW, VLPO, LC	Sleep-Promoting, analgesia	2%	2h	ZT12	Up-regulated	Lu J, et al.,(2008) [13]
AP	Nausea, vomiting	1.3%,2.6%	2h	/	Up-regulated	Hase T, et al.,(2019) [58]

Abbreviation: VLPO, Ventrolateral preoptic nucleus; PIR, Piriform area; LSD, Lateral septal nucleus, dorsal part; LSV, Lateral septal nucleus, ventral part; NTS, Nucleus of the solitary tract; VeN, Ventral group of the dorsal thalamus; CeA, Central amygdalar nucleus; SON, Supraoptic nucleus; MnPO, median preoptic nucleus; EW, Edinger-Westphal nucleus; LC, Locus coeruleus; AP, Area postrema.

Supplementary Table 4. Abbreviations of the relevant brain regions in Figure 3.

Region	Abbreviation	Region	Abbreviation	Regio	Abbreviation

				n	
CTX	**Cerebral cortex**	LH	Lateral habenula	OP	Olivary pretectal nucleus
PA	Posterior amygdalar nucleus	SPF	Subparafascicular nucleus	ND	Nucleus of Darkschewitsch
PIR	Piriform area	MH	Medial habenula	VTN	Ventral tegmental nucleus
DG	Dentate gyrus	ATN	Anterior group of the dorsal thalamus	IF	Interfascicular nucleus raphe
ENT	Entorhinal area	VENT	Ventral group of the dorsal thalamus	PPT	Posterior pretectal nucleus
MOB	Main olfactory bulb	LAT	Lateral group of the dorsal thalamus	MRNm	Midbrain reticular nucleus, magnocellular part
CA	Ammon's horn	GENd	Geniculate group, dorsal thalamus	MRNmg	Midbrain reticular nucleus, magnocellular part, general
AON	Anterior olfactory nucleus	RT	Reticular nucleus of the thalamus	MRNp	Midbrain reticular nucleus, parvicellular part
TT	Taenia tecta	SPA	Subparafascicular area	INC	Interstitial nucleus of Cajal
ECT	Ectorhinal area	PP	Peripeduncular nucleus	CS	Superior central nucleus raphe
RSP	Retrosplenial area	PIN	Pineal body	**HB**	**Hindbrain**
ILA	Infralimbic area	**HY**	**Hypothalamus**	NTS	Nucleus of the solitary tract
SUB	Subiculum	SO	Supraoptic nucleus	PB	Parabrachial nucleus
TEa	Temporal association areas	PVH	Paraventricular hypothalamic nucleus	PG	Pontine gray
COA	Cortical amygdalar area	LHA	Lateral hypothalamic area	VNC	Vestibular nuclei
ORB	Orbital area	MPO	Medial preoptic area	GRN	Gigantocellular reticular nucleus
SS	Somatosensory areas	AHN	Anterior hypothalamic nucleus	LRN	Lateral reticular nucleus
MO	Somatomotor areas	SBPV	Subparaventricular zone	PCG	Pontine central gray
VIS	Visual areas	DMH	Dorsomedial nucleus of the hypothalamus	PRNc	Pontine reticular nucleus, caudal part
PERI	Perirhinal area	TU	Tuberal nucleus	IRN	Intermediate reticular nucleus
AUD	Auditory areas	SCH	Suprachiasmatic nucleus	MDRN	Medullary reticular nucleus
AOB	Accessory olfactory bulb	PH	Posterior hypothalamic nucleus	AP	Area postrema
EP	Endopiriform nucleus	ARH	Arcuate hypothalamic nucleus	PRNr	Pontine reticular nucleus

BMAp	Basomedial amygdalar nucleus, posterior part	LPO	Lateral preoptic area	NLL	Nucleus of the lateral lemniscus
TR	Postpiriform transition area	RCH	Retrochiasmatic area	DMX	Dorsal motor nucleus of the vagus nerve
BLA	Basolateral amygdalar nucleus	VMH	Ventromedial hypothalamic nucleus	TRN	Tegmental reticular nucleus
PL	Prelimbic area	VLPO	Ventrolateral preoptic nucleus	CN	Cochlear nuclei
ACA	Anterior cingulate area	PVpo	Periventricular hypothalamic nucleus, preoptic part	DCN	Dorsal column nuclei
LA	Lateral amygdalar nucleus	MPN	Medial preoptic nucleus	PAS	Parasolitary nucleus
DP	Dorsal peduncular area	PVi	Periventricular hypothalamic nucleus, intermediate part	PGRN	Paragigantocellular reticular nucleus
PAA	Piriform-amygdalar area	ZI	Zona incerta	PARN	Parvicellular reticular nucleus
POST	Postsubiculum	MEPO	Median preoptic nucleus	LC	Locus ceruleus
AI	Agranular insular area	AVPV	Anteroventral periventricular nucleus	SPVI	Spinal nucleus of the trigeminal, interpolar part
BMAa	Basomedial amygdalar nucleus, anterior part	MBO	Mammillary body	PHY	Perihypoglossal nuclei
PAR	Parasubiculum	PVa	Periventricular hypothalamic nucleus, anterior part	NI	Nucleus incertus
NLOT	Nucleus of the lateral olfactory tract	PVHd	Paraventricular hypothalamic nucleus, descending division	LDT	Laterodorsal tegmental nucleus
PRE	Presubiculum	PSTN	Parasubthalamic nucleus	V	Motor nucleus of trigeminal
PTLp	Posterior parietal association areas	PVp	Periventricular hypothalamic nucleus, posterior part	DTN	Dorsal tegmental nucleus
GU	Gustatory areas	ADP	Anterodorsal preoptic nucleus	B	Barrington's nucleus
CLA	Claustrum	PMv	Ventral premammillary	SPVC	Spinal nucleus of the

			nucleus		trigeminal, caudal part
FRP	Frontal pole, cerebral cortex	AVP	Anteroventral preoptic nucleus	MARN	Magnocellular reticular nucleus
IG	Induseum griseum	PMd	Dorsal premammillary nucleus	XII	Hypoglossal nucleus
VISC	Visceral area	PS	Parastrial nucleus	SOC	Superior olivary complex
6b	Layer 6b, isocortex	OV	Vascular organ of the lamina terminalis	SLD	Sublaterodorsal nucleus
FC	Fasciola cinerea	STN	Subthalamic nucleus	AMB	Nucleus ambiguus
CNU	**Cerebral nuclei**	SFO	Subfornical organ	VII	Facial motor nucleus
BST	Bed nuclei of the stria terminalis	PD	Posterodorsal preoptic nucleus	NTB	Nucleus of the trapezoid body
CEA	Central amygdalar nucleus	PST	Preparasubthalamic nucleus	SPVO	Spinal nucleus of the trigeminal, oral part
LSr	Lateral septal nucleus, rostral (rostroventral) part	ASO	Accessory supraoptic group	RPO	Nucleus raphe pontis
SI	Substantia innominata	AHA	Anterior hypothalamic area	RO	Nucleus raphe obscurus
NDB	Diagonal band nucleus	PSCH	Suprachiasmatic preoptic nucleus	IO	Inferior olivary complex
ACB	Nucleus accumbens	IPN	Interpeduncular nucleus	SUT	Supratrigeminal nucleus
MS	Medial septal nucleus	**MB**	**Midbrain**	RM	Nucleus raphe magnus
OT	Olfactory tubercle	ICc	Inferior colliculus, central nucleus	LIN	Linear nucleus of the medulla
LSc	Lateral septal nucleus, caudal (caudodorsal) part	SCsg	Superior colliculus, superficial gray layer	x	Nucleus x
AAA	Anterior amygdalar area	ICe	Inferior colliculus, external nucleus	PSV	Principal sensory nucleus of the trigeminal
FS	Fundus of striatum	SCig	Superior colliculus, motor related, intermediate gray layer	y	Nucleus y
MA	Magnocellular nucleus	ICd	Inferior colliculus, dorsal nucleus	SLC	Subceruleus nucleus
IA	Intercalated amygdalar	SCzo	Superior colliculus, zonal layer	ECU	External cuneate nucleus

	nucleus				
MEA	Medial amygdalar nucleus	SCdg	Superior colliculus, motor related, deep gray layer	VI	Abducens nucleus
CP	Caudoputamen	SCop	Superior colliculus, optic layer	RPA	Nucleus raphe pallidus
SF	Septofimbrial nucleus	EW	Edinger-Westphal nucleus	LTN	Lateral tegmental nucleus
BA	Bed nucleus of the accessory olfactory tract	PRC	Precommissural nucleus	PRNv	Pontine reticular nucleus, ventral part
SH	Septohippocampal nucleus	SCiw	Superior colliculus, motor related, intermediate white layer	SG	Supragenual nucleus
GPe	Globus pallidus, external segment	MPT	Medial pretectal area	SSN	Superior salivatory nucleus
TRS	Triangular nucleus of septum	VTA	Ventral tegmental area	z	Nucleus z
BAC	Bed nucleus of the anterior commissure	DR	Dorsal nucleus raphe	ACVI	Accessory abducens nucleus
GPi	Globus pallidus, internal segment	NPC	Nucleus of the posterior commissure	ACVII	Accessory facial motor nucleus
LSv	Lateral septal nucleus, ventral part	APN	Anterior pretectal nucleus	EV	Efferent vestibular nucleus
PVT	Paraventricular nucleus of the thalamus	SNr	Substantia nigra, reticular part	ECO	Efferent cochlear group
TH	**Thalamus**	NOT	Nucleus of the optic tract	ICB	Infracerebellar nucleus
RE	Nucleus of reuniens	CLI	Central linear nucleus raphe	ISN	Inferior salivatory nucleus
GENv	Geniculate group, ventral thalamus	RL	Rostral linear nucleus raphe	PMR	Paramedian reticular nucleus
ILM	Intralaminar nuclei of the dorsal thalamus	SNc	Substantia nigra, compact part	PPY	Parapyramidal nucleus
PT	Parataenial nucleus	SCdw	Superior colliculus, motor related, deep white layer	INV	Interstitial nucleus of the vestibular nerve
MED	Medial group of the dorsal thalamus	RN	Red nucleus	SIMmo	Simple lobule, molecular layer

Supplementary Table 5. The brain regions used for functional network analysis in Figure 6.

	CTX	Cerebral cortex		HY	Hypothalamus
1	ACA	Anterior cingulate area	32	ARH	Arcuate hypothalamic nucleus
2	AI	Agranular insular area	33	LHA	Lateral hypothalamic area
3	AUD	Auditory areas	34	LPO	Lateral preoptic area
4	CA	Ammon's horn	35	MBO	Mammillary body
5	COA	Cortical amygdalar area	36	MEPO	Median preoptic nucleus
6	DG	Dentate gyrus	37	MPN	Medial preoptic nucleus
7	ECT	Ectorhinal area	38	MPO	Medial preoptic area
8	ENT	Entorhinal area	39	PVH	Paraventricular hypothalamic nucleus
9	ILA	Infralimbic area	40	PVi	Periventricular hypothalamic nucleus, intermediate part
10	MO	Somatomotor areas	41	SO	Supraoptic nucleus
11	MOB	Main olfactory bulb	42	STN	Subthalamic nucleus
12	ORB	Orbital area	43	TU	Tuberal nucleus
13	PIR	Piriform area	44	VLPO	Ventrolateral preoptic nucleus
14	PL	Prelimbic area	45	ZI	Zona incerta
15	RSP	Retrosplenial area		MB	Midbrain
16	SS	Somatosensory areas	46	APN	Anterior pretectal nucleus
17	TEa	Temporal association areas	47	DR	Dorsal nucleus raphe
18	TT	Taenia tecta	48	EW	Edinger-Westphal nucleus
19	VIS	Visual areas	49	PAG	Periaqueductal gray
	CNU	Cerebral nuclei	50	RR	Midbrain reticular nucleus, retrorubral area
20	ACB	Nucleus accumbens	51	SNr	Substantia nigra, reticular part
21	BST	Bed nuclei of the stria terminalis	52	VTA	Ventral tegmental area
22	CEA	Central amygdalar nucleus	53	MRN	Midbrain reticular nucleus
23	LSc	Lateral septal nucleus, caudal (caudodorsal) part	54	PPN	Pedunculopontine nucleus
24	LSr	Lateral septal nucleus, rostral (rostroventral) part		HB	Hindbrain
25	OT	Olfactory tubercle	55	CS	Superior central nucleus raphe
26	MS	Medial septal nucleus	56	LC	Locus ceruleus
	TH	Thalamus	57	NTS	Nucleus of the solitary tract
27	LAT	Lateral group of the dorsal	58	PB	Parabrachial nucleus

		thalamus			
28	LH	Lateral habenula	59	PCG	Pontine central gray
29	PVT	Paraventricular nucleus of the thalamus	60	SLD	Sublaterodorsal nucleus
30	RE	Nucleus of reunions	61	TRN	Tegmental reticular nucleus
31	RT	Reticular nucleus of the thalamus	62	LDT	Laterodorsal tegmental nucleus
			63	PRNr	Pontine reticular nucleus（PRNr）

920

A

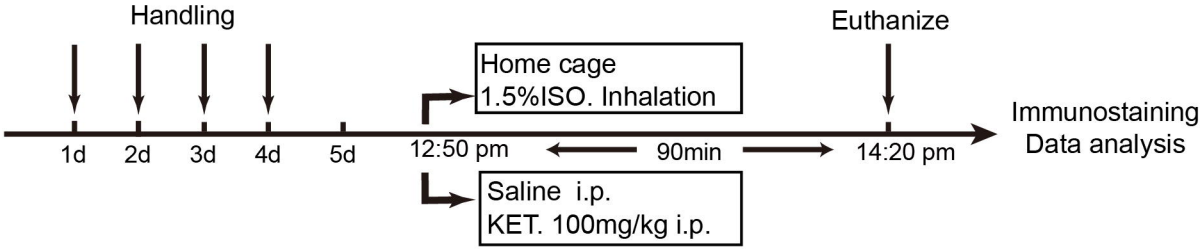
Handling
Euthanize
Home cage
1.5%ISO. Inhalation
Immunostaining
Data analysis
1d
2d
3d
4d
5d
12:50 pm
90min
14:20 pm
Saline i.p.
KET. 100mg/kg i.p.

B

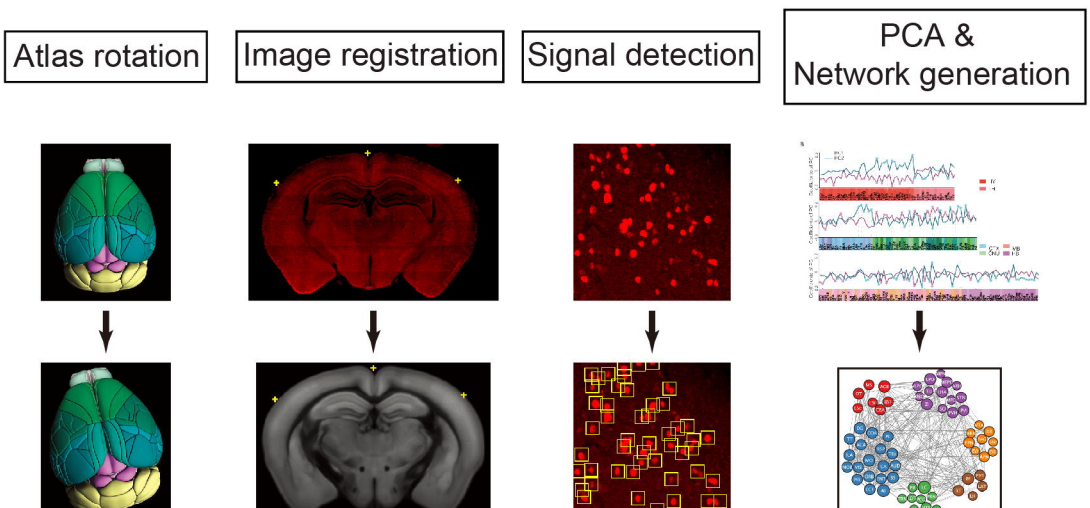
Atlas rotation
Image registration
Signal detection
PCA &
Network generation

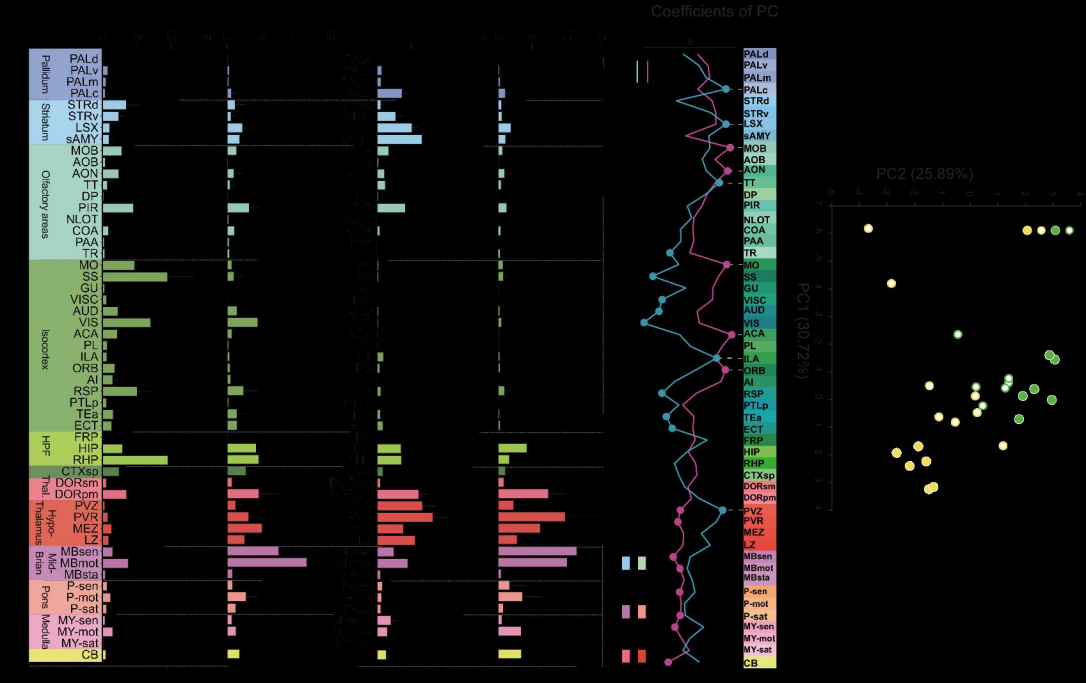
Coefficients of PC
PC1 (30.72%)
PC2 (25.89%)
Pallidum
Striatum
Olfactory areas
Isocortex
HPF
Thal
Hypo-
Thalamus
Midbrain
Pons
Medulla
PALd
PALv
PALm
PALc
STRd
STRv
LSX
sAMY
MOB
AOB
AON
TT
DP
PIR
NLOT
COA
PAA
TR
MO
SS
GU
VISC
AUD
VIS
ACA
PL
ILA
ORB
AI
RSP
PTLp
TEa
ECT
FRP
HIP
RHP
CTXsp
DORsm
DORpm
PVZ
PVR
MEZ
LZ
MBsen
MBmot
MBsta
P-sen
P-mot
P-sat
MY-sen
MY-mot
MY-sat
CB

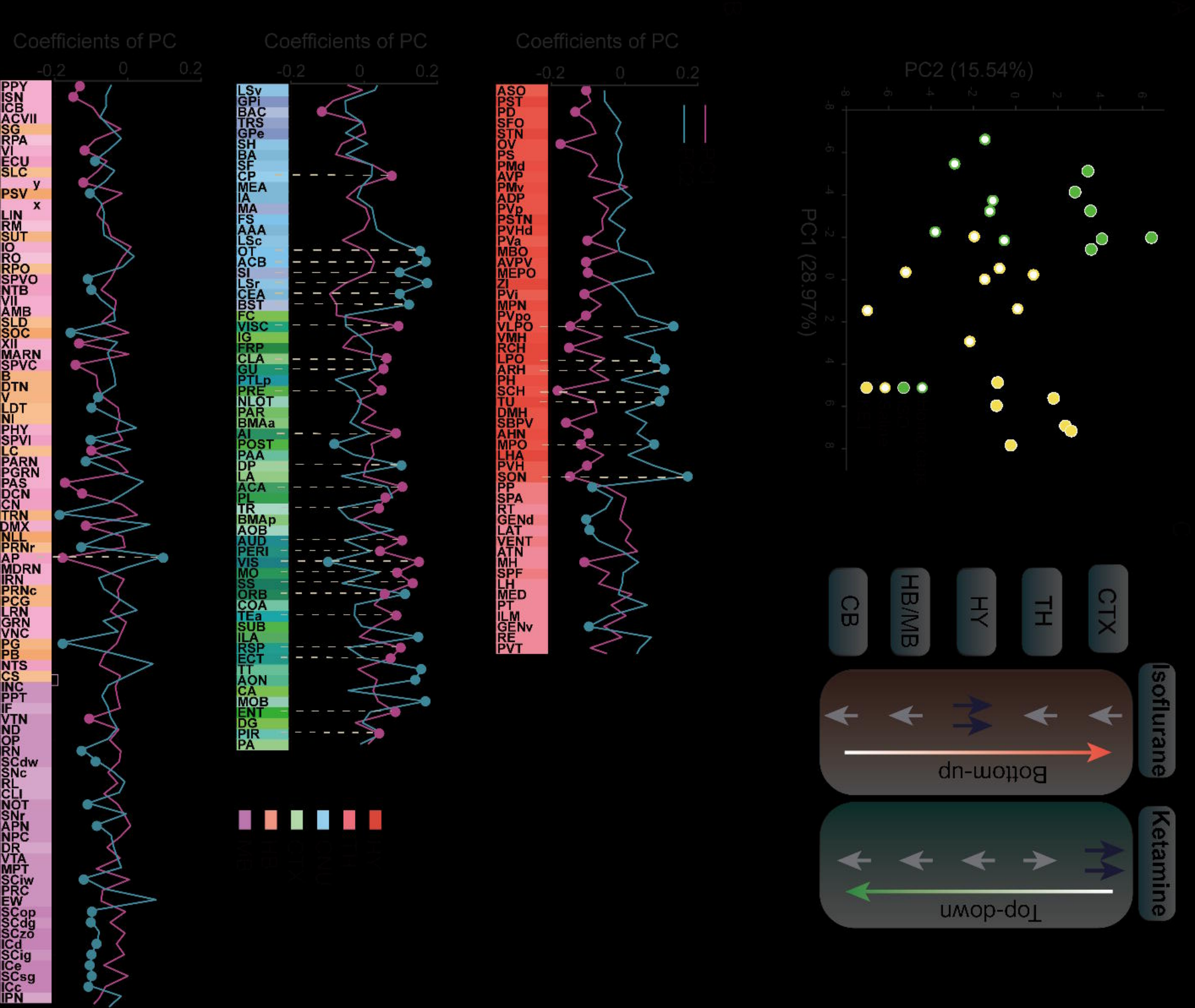
Coefficients of PC
-0.2
0
0.2
PPY
ISN
ICB
ACVII
SG
RPA
VI
ECU
SLC
PSV
y
x
LIN
RM
SUT
IO
RO
RPO
SPVO
NTB
VII
AMB
SLD
SOC
XII
MARN
SPVC
B
DTN
V
LDT
NI
PHY
SPVI
LC
PARN
PGRN
PAS
DCN
CN
TRN
DMX
NLL
PRNr
AP
MDRN
IRN
PRNc
PCG
LRN
GRN
VNC
PG
PB
NTS
CS
INC
PPT
IF
VTN
ND
OP
RN
SCdw
SNc
RL
CLI
NOT
SNr
APN
NPC
DR
VTA
MPT
SCiw
PRC
EW
SCop
SCdg
SCzo
ICd
SCig
ICe
SCsg
ICc
IPN
LSv
GPi
BAC
TRS
GPe
SH
BA
SF
CP
MEA
IA
MA
FS
AAA
LSc
OT
ACB
SI
LSr
CEA
BST
FC
VISC
IG
FRP
CLA
GU
PTLp
PRE
NLOT
PAR
BMAa
AI
POST
PAA
DP
LA
ACA
PL
TR
BMAp
AOB
AUD
PERI
VIS
MO
SS
ORB
COA
TEa
SUB
ILA
RSP
ECT
TT
AON
CA
MOB
ENT
DG
PIR
PA
ASO
PST
PD
SFO
STN
OV
PS
PMd
AVP
PMv
ADP
PVp
PSTN
PVHd
PVa
MBO
AVPV
MEPO
ZI
PVi
MPN
PVpo
VLPO
VMH
RCH
LPO
ARH
PH
SCH
TU
DMH
SBPV
AHN
MPO
LHA
PVH
SON
PP
SPA
RT
GENd
LAT
VENT
ATN
MH
SPF
LH
MED
PT
ILM
GENv
RE
PVT
PC2 (15.54%)
PC1 (28.97%)
CB
HB/MB
HY
TH
CTX
Isoflurane
Bottom-up
Ketamine
Top-down

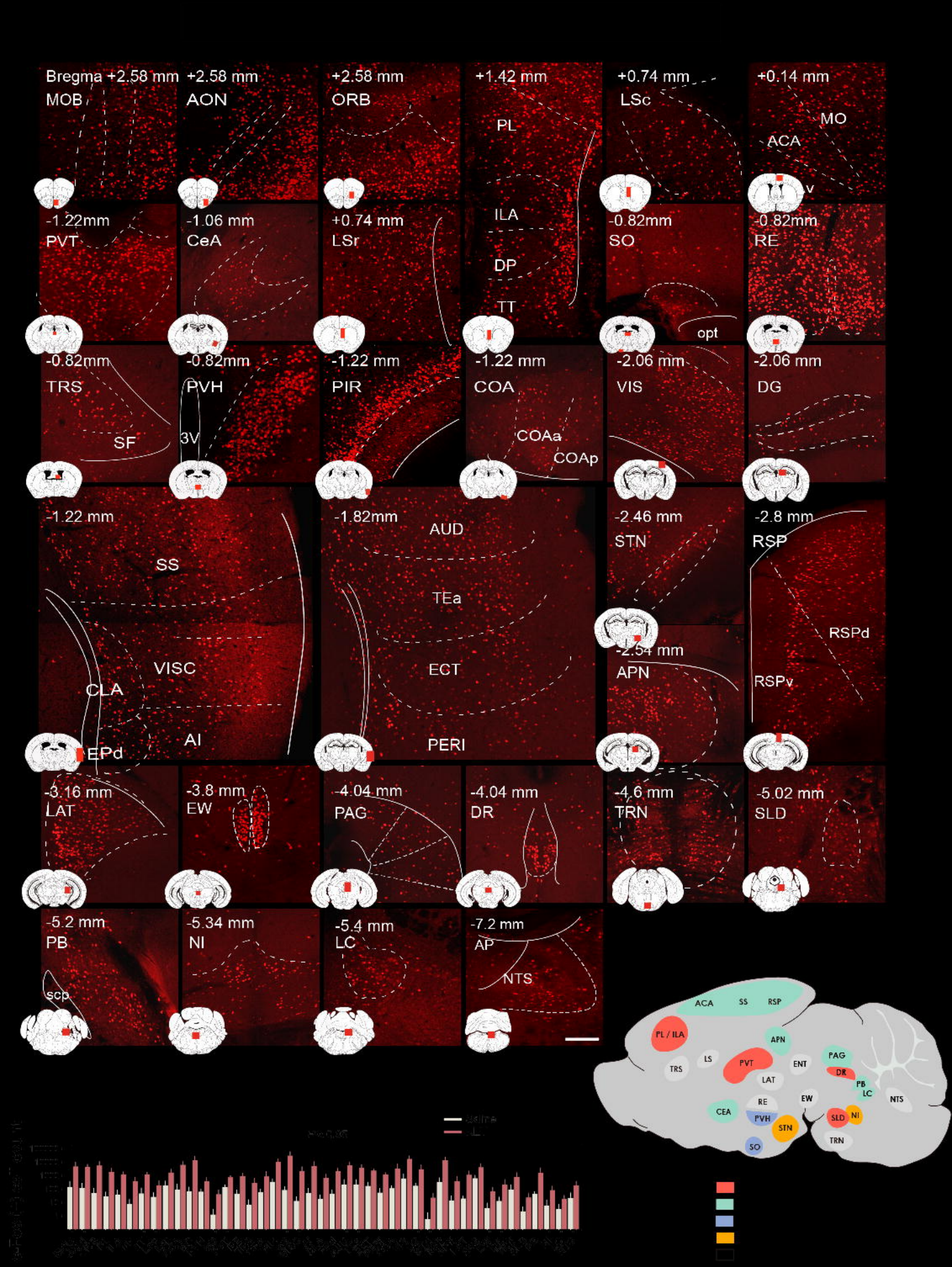
Bregma +2.58 mm
MOB
+2.58 mm
AON
+2.58 mm
ORB
+1.42 mm
PL
ILA
DP
TT
+0.74 mm
LSc
+0.14 mm
MO
ACA
V
-1.22mm
PVT
-1.06 mm
CeA
+0.74 mm
LSr
-0.82mm
SO
-0.82mm
RE
opt
-0.82mm
TRS
SF
-0.82mm
PVH
3V
-1.22 mm
PIR
-1.22 mm
COA
COAa
COAp
-2.06 mm
VIS
-2.06 mm
DG
-1.22 mm
SS
VISC
CLA
EPd
AI
-1.82mm
AUD
TEa
ECT
PERI
-2.46 mm
STN
-2.8 mm
RSP
RSPd
RSPv
-2.54 mm
APN
-3.16 mm
LAT
-3.8 mm
EW
-4.04 mm
PAG
-4.04 mm
DR
-4.6 mm
TRN
-5.02 mm
SLD
-5.2 mm
PB
scp
-5.34 mm
NI
-5.4 mm
LC
-7.2 mm
AP
NTS
ACA
SS
RSP
PL / ILA
APN
TRS
LS
PVT
ENT
PAG
DR
LAT
PB
LC
NTS
RE
EW
CEA
PVH
STN
SLD
NI
SO
TRN

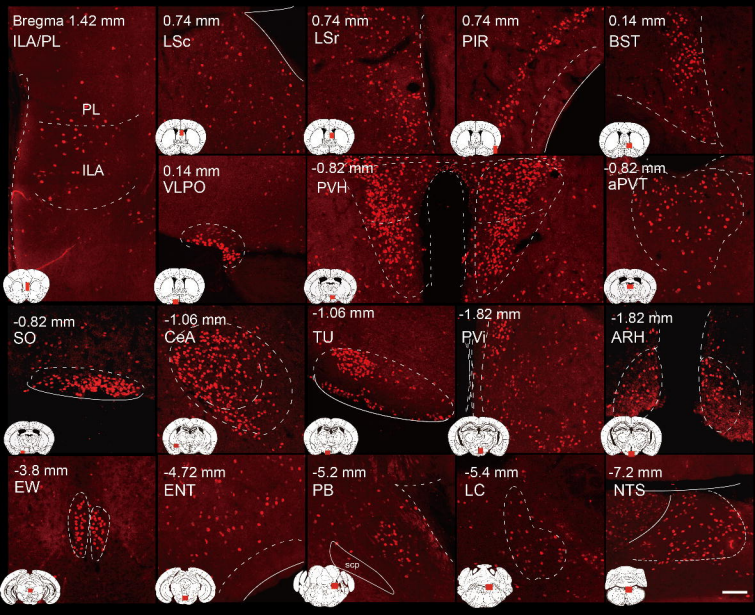
Bregma 1.42 mm
ILA/PL
PL
ILA
0.74 mm
LSc
0.74 mm
LSr
0.74 mm
PIR
0.14 mm
BST
0.14 mm
VLPO
-0.82 mm
PVH
-0.82 mm
aPVT
-0.82 mm
SO
-1.06 mm
CeA
-1.06 mm
TU
-1.82 mm
PVi
-1.82 mm
ARH
-3.8 mm
EW
-4.72 mm
ENT
-5.2 mm
PB
scp
-5.4 mm
LC
-7.2 mm
NTS

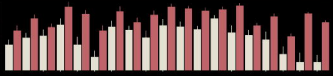

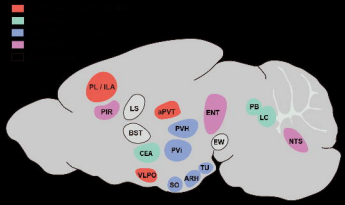
PL / ILA
PIR
LS
aPVT
ENT
PB
LC
BST
PVH
CEA
PVi
EW
NTS
VLPO
SO
ARH
TU

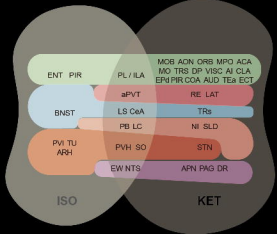
ENT PIR
PL / ILA
MOB AON ORB MPO ACA
MO TRS DP VISC AI CLA
EPI PIR COA AUD TEa ECT
BNST
aPVT
RE LAT
LS CeA
TRs
PB LC
NI SLD
PVi TU
ARH
PVH SO
STN
EW NTS
APN PAG DR
ISO
KET

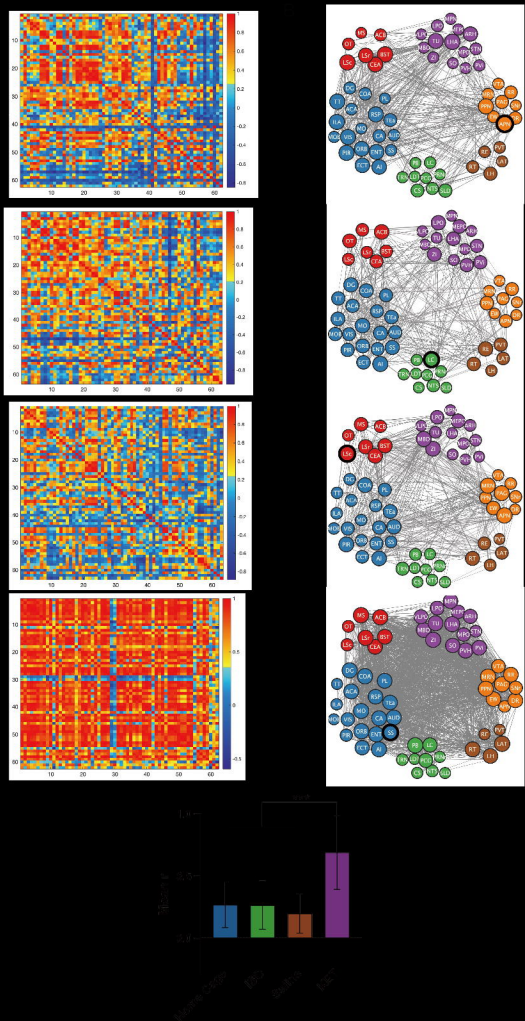

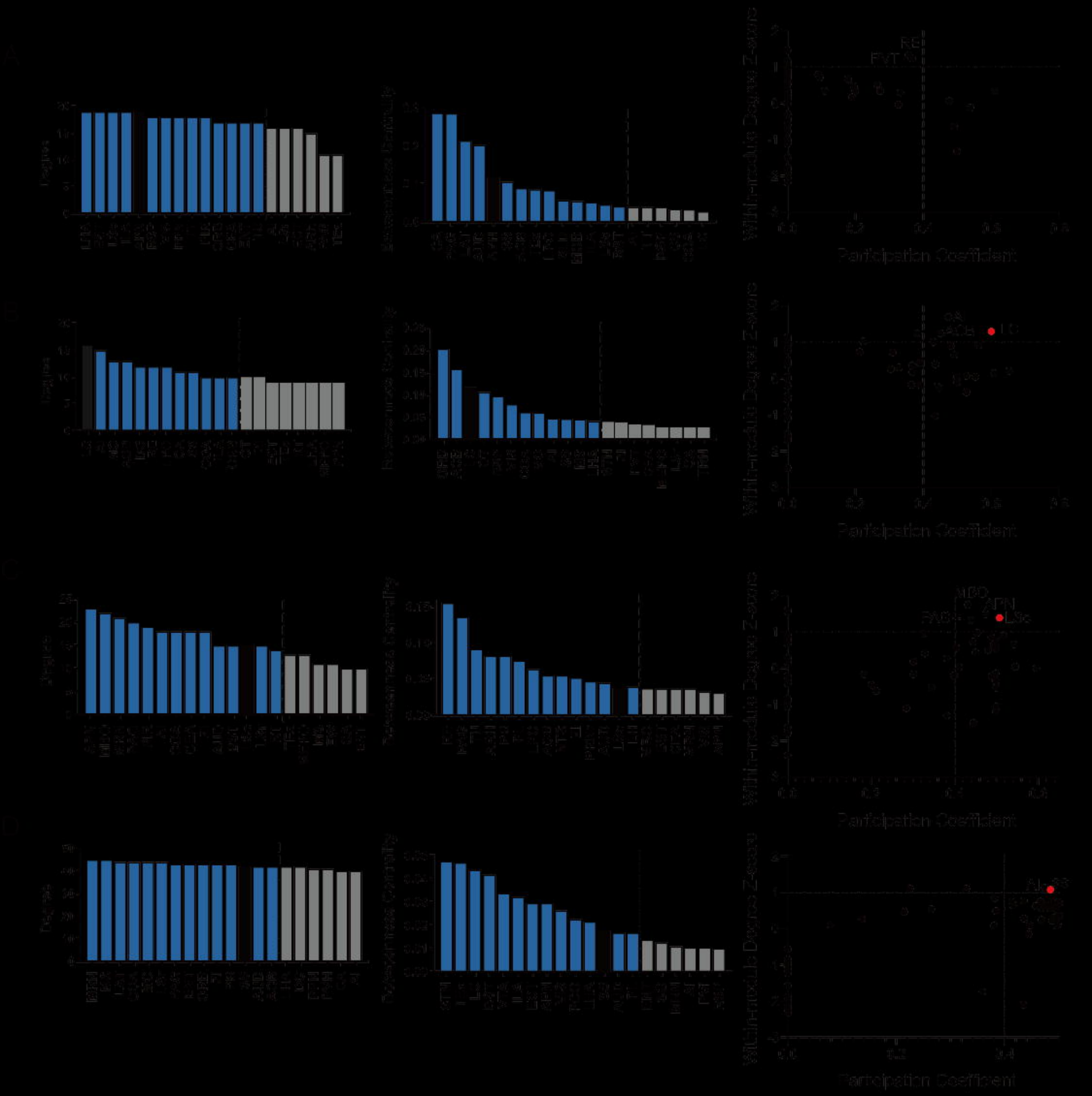

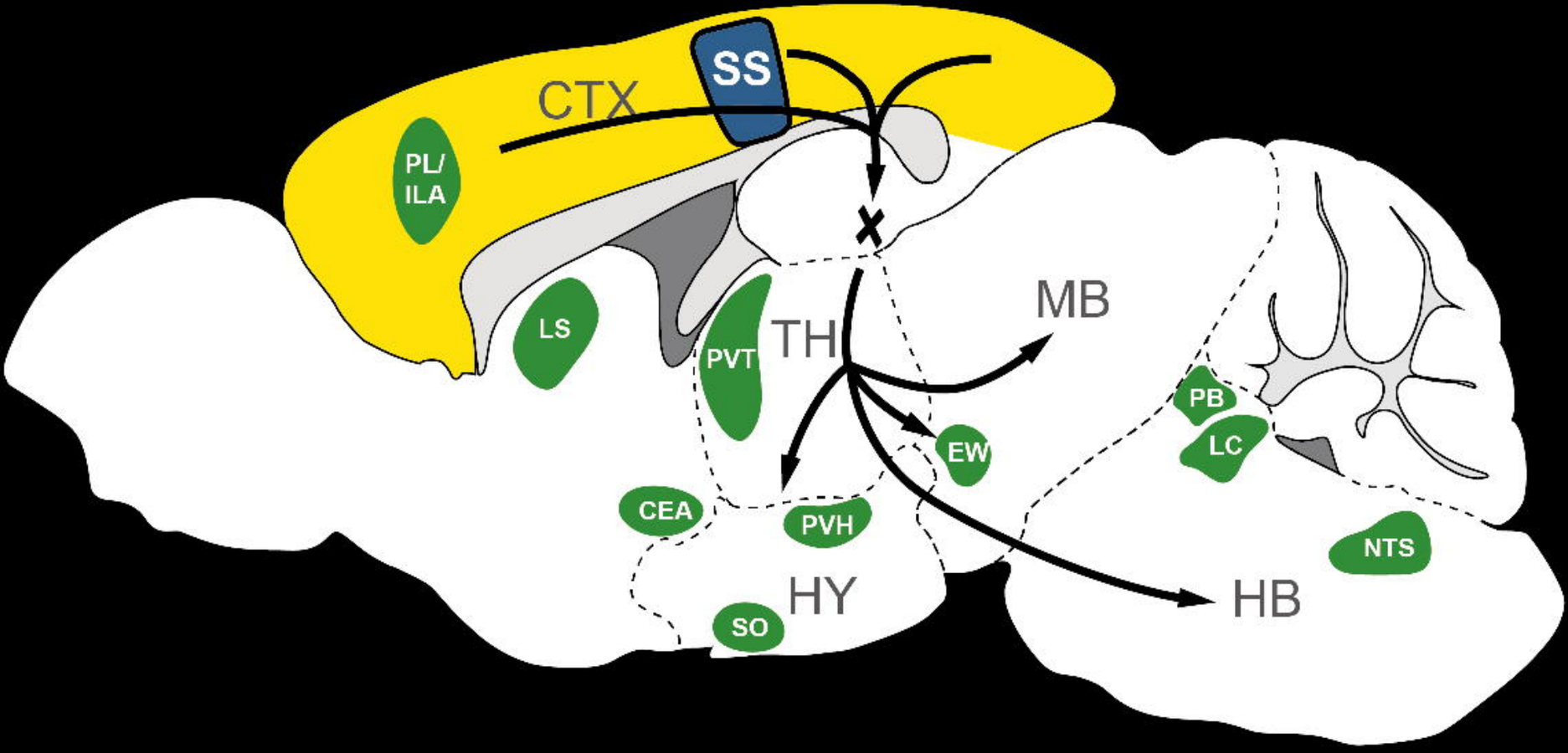
SS
CTX
PL/
ILA
LS
PVT
TH
MB
PB
LC
EW
CEA
PVH
NTS
HY
HB
SO

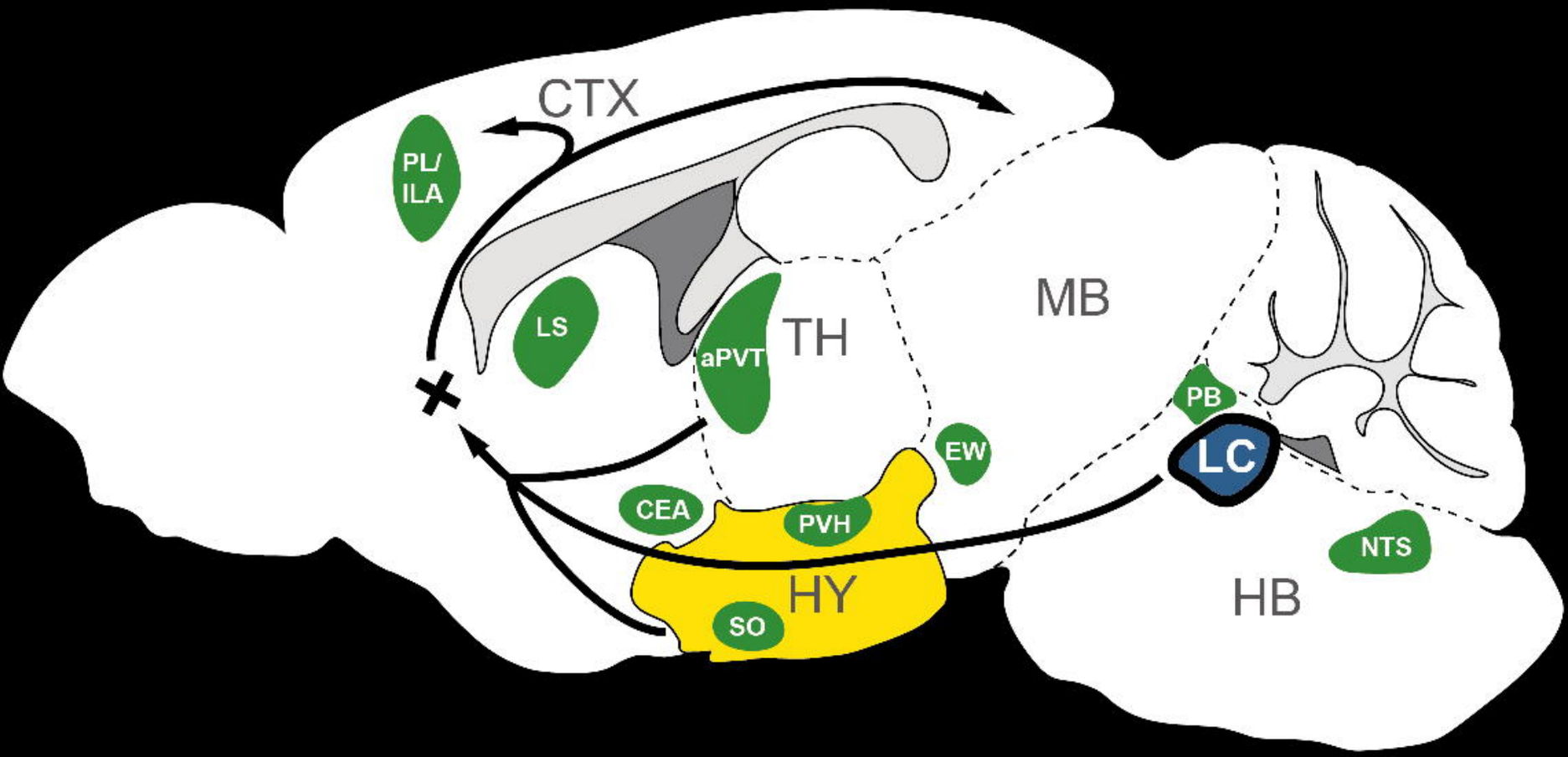
CTX
PL/
ILA
LS
aPVT
TH
MB
PB
LC
EW
CEA
PVH
NTS
HY
HB
SO